

Article

The Impact of Environmental Factors on the Thermal Characteristic of a Lithium–ion Battery

Gerd Liebig *, Ulf Kirstein, Stefan Geißendörfer , Omio Zahid, Frank Schuldt  and Carsten Agert 

DLR Institute of Networked Energy Systems, 26123 Oldenburg, Germany; Ulf.Kirstein@dlr.de (U.K.); Stefan.Geissendoerfer@dlr.de (S.G.); omio.zahid@hotmail.com (O.Z.); Frank.Schuldt@dlr.de (F.S.); Carsten.Agert@dlr.de (C.A.)

* Correspondence: gerd.liebig@dlr.de; Tel.: +49-441-99906-423

Received: 29 November 2019; Accepted: 30 December 2019; Published: 2 January 2020;
Corrected: 23 October 2023



Abstract: To draw reliable conclusions about the thermal characteristic of or a preferential cooling strategy for a lithium–ion battery, the correct set of thermal input parameters and a detailed battery layout is crucial. In our previous work, an electrochemical model for a commercially-available, 40 Ah prismatic lithium–ion battery was validated under heuristic temperature dependence. In this work the validated electrochemical model is coupled to a spatially resolved, three dimensional (3D), thermal model of the same battery to evaluate the thermal characteristics, i.e., thermal barriers and preferential heat rejection patterns, within common environment layouts. We discuss to which extent the knowledge of the batteries’ interior layout can be constructively used for the design of an exterior battery thermal management. It is found from the study results that: (1) Increasing the current rate without considering an increased heat removal flux at natural convection at higher temperatures will lead to increased model deviations; (2) Centralized fan air-cooling within a climate chamber in a multi cell test arrangement can lead to significantly different thermal characteristics at each battery cell; (3) Increasing the interfacial surface area, at which preferential battery interior and exterior heat rejection match, can significantly lower the temperature rise and inhomogeneity within the electrode stack and increase the batteries’ lifespan.

Keywords: lithium–ion battery; battery modeling; electrochemical–thermal model; finite element method; model parameterization; model validation; thermal performance analysis; battery thermal management system; cooling strategies

1. Introduction

Lithium–ion batteries that are manufactured without consideration of thermal performance characteristics and optimal specifications with respect to the battery systems application might fail at an early stage in their expected product lifetime [1–3]. A strong correlation between battery temperature and battery degradation is reported for battery performance in the literature [2–7]. Therefore, the research on battery degradation induced by temperature effects is a vital multidisciplinary field with research branches in battery temperature monitoring and regulation [3,4,8], battery performance prediction [9–15] and optimization [8,16,17], as well as battery system design [1,18–20]. The shared aim is to decrease the impact of temperature-induced fault mechanisms and battery cell performance flaws within the associated battery system, while, as the applications demand, safety objectives and durability ambitions are met [17,21,22].

From a physics point of view, the thermal characteristic of a lithium–ion battery within the system is a balance between heat generated and incorporated within its encapsulated electrode stack, and

the current conducting components against heat removal by an interior or exterior heat rejection method [3,6,23].

Heat generation within the electrode stack relates to irreversible sources connected to internal resistance [24,25] contributions by ionic, electrical and interfacial phenomena, reversible sources connected to entropy [14,26] and the heat of mixing [27,28]. Heat incorporation is a passive phenomenon quantified by material heat capacity [29–31]. Interior design improvements in heat removal are reported for electrode and stack modification with the focus on the minimizing of internal resistance contributions, enhancing thermal conductivity on a material level [32], or within the stack arrangement [33], as well as the customizing of the battery tap [34–36] and the terminal layout [37]. Exterior design cooling types in general embrace air [38–40], liquid [41,42], heat pipe [3,43], phase change material (PCM) [44,45] or hybrids [18,46] with a focus on multiple cell arrangements and interconnects under the influence of system application and management.

Modeling of the thermal aspects of lithium-ion battery operation states relies on model parameterization [47–50], validation of key performance variables [21,47,51,52] and the correct interpretation of model deviations [53,54], as well as behavioral indicators [55]. Therefore, the model accuracy strongly depends on the accurate modeling of each of the aforementioned physical phenomena that influences the flux of heat within and around the battery cell.

In our previous study [47] an electrochemical thermal coupled model was established based on the COMSOL Multiphysics® simulation platform (Stockholm, Sweden) and validated dependent upon heuristic cell temperature without the geometrically resolved battery and test environment. The present study aims to get a thorough understanding of the thermal processes and their implications within and around a prismatic (PHEV2) battery cell to evaluate the layout of thermal barriers and preferential heat rejection patterns within controlled validation scenarios. Finally, the parameterized model is adopted to analyze conductive cooling strategies considered in a recent market ready battery thermal management system (BTMS) under variable battery form factors with similar thermal characteristics.

2. Methods

2.1. Experimental Techniques

The model parameterization involves multiple steps from battery cell disassembly, sample extraction and preparation, measurement execution and data evaluation [48,52,53,56,57]. The opening and sample preparation from a discharged battery cell with a zero state of charge was explained and discussed in detail in our previous study with its focus on the electrochemical model parameterization [47]. In this study the focus is set on the thermal model parameterization.

2.1.1. Battery Description

For model parameterization, a commercially-available PHEV2 battery of a nickel–manganese–cobalt (NMC)/graphite (G) type was used. The cell has a nominal theoretical capacity of 40 Ah and 144 Wh, measured at 1/3 C constant current rate. Thereby, 1 C equals an applied current of 40 A. A voltage range between 2.8 V to 4.2 V is recommended by the manufacturer with a nominal voltage of 3.6 V. Charging is allowed within a temperature range of 0 °C to 45 °C up to a maximal discharge current rate of 5 C, while discharging is approved up to 10 °C within –20 °C to 55 °C.

2.1.2. Thermal Parameter Assessment

The heat capacity C_p and the temperature diffusivity α for each component of the electrode stack were measured by Differential Scanning Calorimetry (DSC 204 F1, Netzsch, Selb, Germany) and Laser Flash Analysis (LFA 467, Netzsch, Germany), respectively. The characterized cell component categories comprised a double coated graphite anode on copper foil, double coated NMC cathode on aluminum foil and a separator sheet.

The DSC device setup and measurement fundamentals for the heat capacity evaluation are described by Höhne et al. [58]. Coating material is removed from the electrodes metal foil by a scalpel. Separator sheets were sliced into small pieces. Each material was loaded into a separate pierced aluminum crucible.

The measurement parameters were defined within DSC phoenix software (Netzsch, Germany) to be within a temperature range of 25 °C to 80 °C and with a heating rate of 10 K/min. As a reference, a baseline correction measurement was executed with an empty crucible and a calibration measurement was performed with a sapphire standard of 12.73 mg, thickness of 0.25 mm and a diameter of 4 mm. The final heat capacity analysis is done within Proteus Analysis software (Netzsch, Germany) to access the heat capacity values needed for further modeling steps.

The principle of the LFA measurement and evaluation procedure is described by Parker et al. [59]. Applications of the methods for the characterization of lithium–ion battery components were demonstrated by Bohn et al. [21] and Koo et al. [33]. The laser flash technique directly measures the sample's temperature diffusivity. Each sample is placed into a stage. A xenon flash lamp heats the samples surface, while the temperature rise is measured on the other side with an InSb infrared (IR) detector. Within the thermal diffusivity measurements, all samples were measured with 270 V for 0.5 ms at temperatures between room temperature and 80 °C (5 °C steps). The separator was coated with a homogenous thin graphite layer prior to its measurement to avoid energy loss of the laser by reflection at the separators surface. The anisotropic thermal conductivity k of the electrode stack was approximated by Equations (10) and (11) based on the sample results.

2.1.3. Thermal Validation Assessment

The validation tests were performed by a Maccor series 4000 Potentiostat multiple cell tester with 0 V to 8 V (0.02% accuracy) range for the voltage and 0 A to 150 A range for the current (0.05% accuracy). The temperature environment was regulated within a Vötsch climate chamber, VC 7018 with a temperature range of −75 °C to 180 °C, by air circulation to control the applied measurement conditions. An Agilent 34972A with PT100 sensors, having a −40 °C to 85 °C (± 0.1 K accuracy) temperature range each, was used to measure the temperature pointwise within the test setup. Climate conditions exterior to the climate chamber and reflective radiation at the interior chamber surfaces are assumed to have a negligible effect upon the measurements.

Two different experimental test setups of the prismatic battery cell were used to analyze the temperature behavior of the prismatic battery cell type under varying typical environmental and procedural test conditions. The focus of the first validation experiment was the evaluation of localized temperature magnitudes and temperature inhomogeneity at varying current rates under natural convection conditions for the chosen prismatic battery type. Within the second validation experiment the temperature on top of the battery was evaluated during a forced cooling condition at a fixed current rate with varying position within a battery pack-like test arrangement.

Within the first setup, current rates of 0.5 C, 1 C and 2 C, separated discharge and charge phases and an initial temperature set to 25 °C, were considered. Twelve temperature sensors were positioned on the surface of the battery cell on predefined locations. The battery was positioned and fixed with two thermally low, conducting synthetic fasteners. The climate chamber temperature regulation is turned off during the battery cycling processes to avoid undesired cooling effects. After each heating phase, a cooling phase of several hours was considered. Before a new test was initiated, an evenly homogenized temperature distribution was reestablished.

In contrast, the second test setup was composed of six prismatic batteries, which were cycled at 2 C current rate and an environment temperature of 22 °C, a thermally high conducting metal fastener holding each. Thereby, the climate chamber is actively fan cooling the test arrangement, while the battery cells are not directly electrically connected to each other. Three electrical and thermal battery cell profiles were chosen for the further evaluation based on their location in the center, middle and side positions within the test arrangement.

2.2. Simulation Techniques

The developed model is implemented in the COMSOL Multiphysics® v5.4 simulation platform using the “Lithium-ion Battery” submodule for the definition of the electrochemical behavior and the “Heat Transfer in Solids and Fluids” submodule to describe the thermal behavior within the battery and the test environment.

The governing set of equations for the electrochemistry and the evaluation of heat dissipations sources are denoted in Tables A1 and A2 in the Appendix A, since the focus in this paper is on external influences on the thermal characteristics of the battery cell. The schematic of the model implemented is shown in Figure 1, where the material property representatives annotated within the electrochemical model are the negative electrode coating layer (ne), the positive electrode coating layer (pe), the separator layer (sep) and the current collecting layers (cc-cu) and (cc-al):

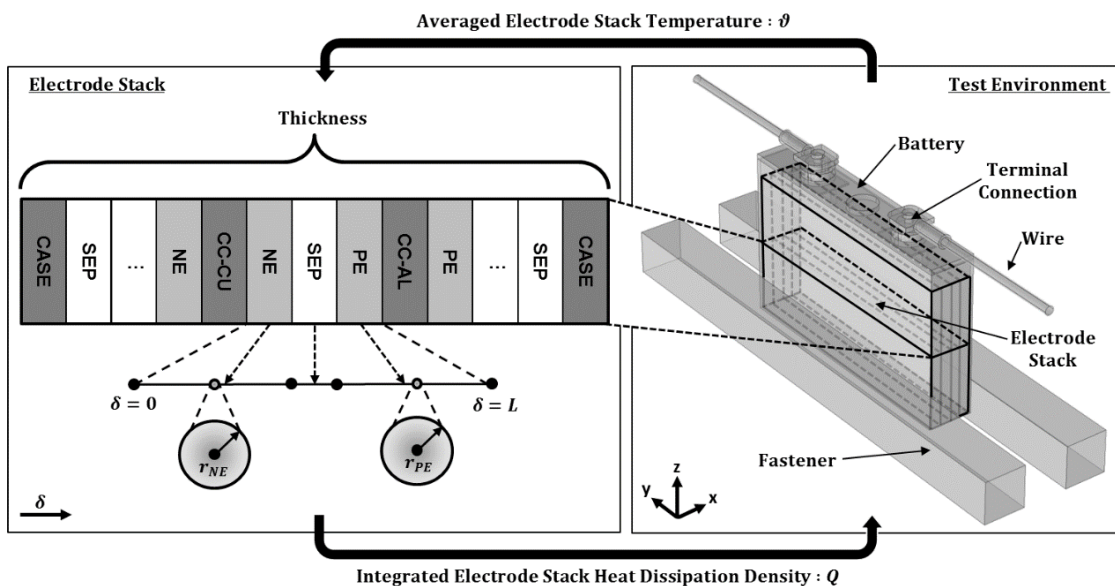


Figure 1. Schematics of the lithium–ion battery and heat transfer model.

2.2.1. Heat Transfer in Solids

The heat propagation within solid domains $V \subset \mathbb{R}^3$ at position $s = (x, y, z) \in V$ and time $t \in T = [0, \tau], \tau > 0$, is calculated by the transient heat transfer equation as follows:

$$\underbrace{\rho(s) C_p(s, \vartheta(t, s)) \frac{\partial \vartheta(t, s)}{\partial t}}_{\text{Diffusion}} - \underbrace{\nabla \cdot (k(s, \vartheta(t, s)) \nabla \vartheta(t, s))}_{\text{Conduction}} = \underbrace{\begin{cases} Q(s, I(t), \vartheta_{avg}(t)) & , s \in U \\ 0 & , s \notin U \end{cases}}_{\text{Heat Source}} \quad (1)$$

where $\vartheta : T \times V \rightarrow \mathbb{R}$ is the temperature, $Q : U \times \mathbb{R} \times \mathbb{R} \rightarrow \mathbb{R}$ is the heat dissipation density dependent on average temperature $\vartheta_{avg}(t) = \text{avg}_{s \in U} \vartheta(t, s)$ within the electrode stack volume $U \subset \mathbb{R}^3$ and applied current $I : T \rightarrow \mathbb{R}$ within the electrochemical model, $\rho : V \rightarrow \mathbb{R}$ is density, $C_p : V \times \mathbb{R} \rightarrow \mathbb{R}$ is temperature-dependent, specific heat capacity under constant pressure, and $k : V \times \mathbb{R} \rightarrow \mathbb{R}^{3 \times 3}$ is the thermal conductivity matrix. The matrix components of k are modeled direction- and temperature-dependent in the case of the electrode stack U , as discussed in Section 2.2.5, and direction- and temperature-independent in any other solid domain. The equation is applied in the solid domain of the battery and the experimental setup. Joule heating at current conducting components beside the electrode stack is neglected in this study.

2.2.2. Heat Transfer in Fluids

The heat propagation within the fluid domain $F \subset \mathbb{R}^3$ surrounding the experimental setup is considered at position $s = (x, y, z) \in F$ and time $t \in T = [0, \tau]$, $\tau > 0$, as follows:

$$\rho(s, \vartheta(t, s)) C_p(s, \vartheta(t, s)) \left(\underbrace{\frac{\partial \vartheta(t, s)}{\partial t}}_{\text{Diffusion}} + \underbrace{\vec{u}(t, s) \cdot \nabla \vartheta(t, s)}_{\text{Advection}} - \nabla \cdot (k(s, \vartheta(t, s)) \nabla \vartheta(t, s)) \right) = 0 \quad (2)$$

where $\vartheta : T \times F \rightarrow \mathbb{R}$ is the temperature, $\rho : F \times \mathbb{R} \rightarrow \mathbb{R}$ is the density, $C_p : F \times \mathbb{R} \rightarrow \mathbb{R}$ is the specific heat capacity under constant pressure and $k : F \times \mathbb{R} \rightarrow \mathbb{R}^{3 \times 3}$ is the thermal conductivity matrix. The vector $\vec{u} : T \times F \rightarrow \mathbb{R}^3$ describes airstream velocity within the fluid domain F . Each of the fluid domain's material parameters are modeled temperature-dependent. Work induced by temperature-dependent pressure is neglected.

2.2.3. Convection

The heat transferred via convection is usually considered on a boundary $S = \partial V \subset \mathbb{R}^2$ of a solid volume $V \subset \mathbb{R}^3$ pointwise for $s \in S$ by the following Robin condition:

$$-\vec{n}_S(s) \cdot (k(s, \vartheta(t, s)) \nabla \vartheta(t, s)) = h (\vartheta(t, s) - \vartheta_{ext}) \quad (3)$$

Therein, $\vec{n}_S : S \rightarrow \mathbb{R}^3$ is the normalized orthogonal vector associated to the boundary S , $k(s, \vartheta(t, s)) \nabla \vartheta(t, s)$ is the weighted temperature gradient, $\vartheta : T \times V \rightarrow \mathbb{R}$ is the temperature, $\vartheta_{ext} = \text{const.}$ is the temperature of an external domain, and $h = \text{const.}$ is the heat transfer coefficient at the boundary S . Natural convection and forced convection are subcategories with respect to a fluid flow with and without the induced external fluid force. Heat transfer coefficients vary in literature within $0.6 \text{ W m}^{-2} \text{ K}^{-1}$ to $20 \text{ W m}^{-2} \text{ K}^{-1}$ for natural convection and higher for forced convection [60–62], when the fluid is considered to be air. A clearly defined transition zone does not exist, since mixed convection in dependence of temperature, pressure and gravity is known to occur as the superposition of the aforementioned convection types [63].

In many studies, the heat transfer coefficient on the battery surface is considered as a fitting parameter to improve model errors, which could relate to a false interpretation of other battery parameters [53,55]. Instead, in this study, the environment surrounding the battery test arrangement is modeled with stationary equations of both momentum balance Equation (4) and continuity Equation (5), to replicate the weakly compressible fluid flow behavior within the fluid domain $F \subset \mathbb{R}^3$ representing air:

$$\begin{aligned} \rho(s, \vartheta(t, s)) (\vec{u}(t, s) \cdot \nabla) \vec{u}(t, s) &= \underbrace{-p(t, s) I + \mu(s, \vartheta(t, s)) \left(\left(\nabla \vec{u}(t, s) + (\nabla \vec{u}(t, s))^T \right) - \frac{3}{2} (\nabla \cdot \vec{u}(t, s)) I \right)}_{\text{Weakly Compressible Flow}} \\ &= \nabla \cdot \left[-p(t, s) I + \mu(s, \vartheta(t, s)) \left(\left(\nabla \vec{u}(t, s) + (\nabla \vec{u}(t, s))^T \right) - \frac{3}{2} (\nabla \cdot \vec{u}(t, s)) I \right) \right] \end{aligned} \quad (4)$$

$$\nabla \cdot (\rho(s, \vartheta(t, s)) \vec{u}(t, s)) = 0 \quad (5)$$

Therein, $\rho : F \times \mathbb{R} \rightarrow \mathbb{R}$ is density and $\mu : F \times \mathbb{R} \rightarrow \mathbb{R}$ is dynamic viscosity; both being temperature-dependent. The vector $\vec{u} : T \times F \rightarrow \mathbb{R}^3$ is airstream velocity, $p : T \times F \rightarrow \mathbb{R}$ is the pressure variable and I is the identity matrix. The climate chamber fan-induced fluid flow force is modeled at the boundary S_{in} opposite to the battery test arrangement by the following Neumann boundary condition:

$$\vec{u}(s) = -V_{in} \vec{n}_{S_{in}}(s) \quad (6)$$

where $\vec{u} : S_{in} \rightarrow \mathbb{R}^3$ is the velocity vector on the boundary S_{in} , $\vec{n}_{S_{in}} : S_{in} \rightarrow \mathbb{R}^3$ is the normalized orthogonal vector on the boundary S_{in} and $V_{in} = \text{const.}$ is the inlet velocity control parameter.

2.2.4. Radiation

The heat transferred by radiation is considered on a boundary $S = \partial V \subset \mathbb{R}^2$ of a solid volume $V \subset \mathbb{R}^3$ pointwise for $s \in S$ by the following Robin condition:

$$-\vec{n}_S(s) \cdot (k(s, \vartheta(t, s)) \nabla \vartheta(t, s)) = \sigma \epsilon(s) (\vartheta(t, s)^4 - \vartheta_{ext}^4) \quad (7)$$

where $\vec{n}_S : S \rightarrow \mathbb{R}^3$ is the normalized orthogonal vector associated to the boundary S , $k(s, \vartheta(t, s)) \nabla \vartheta(t, s)$ is the weighted temperature gradient, σ is the Stefan-Boltzmann constant, $\epsilon : S \rightarrow \mathbb{R}$ is the emissivity coefficient, $\vartheta : T \times S \rightarrow \mathbb{R}$ is the temperature and $\vartheta_{ext} = \text{const.}$ is the external environment temperature.

2.2.5. Electrode Stack Thermal Behavior

For the electrode stack domain $U \in \mathbb{R}^3$ of the battery, the effective density ρ^{eff} and effective heat capacity C_p^{eff} are calculated based on the volume averaging method: [21]

$$\rho^{eff} = \sum_{j \in J} v_j \rho_j \quad (8)$$

$$C_p^{eff}(\vartheta) = \sum_{j \in J} v_j C_{p,j}(\vartheta) \quad (9)$$

where $v_j = V_j / V_{Stack}$ is the j -th volume fraction, $\rho_j = \text{const.}$ is the j -th density and $C_{p,j} : \mathbb{R} \rightarrow \mathbb{R}$ is the j -th heat capacity of the j -th component within the electrode stack, $j \in J$. The set J contains a representative of each material within the electrode stack: The negative electrode coating (ne), the positive electrode coating (pe), the current collector sheet of the negative electrode (cc-cu), the current collector sheet of the positive electrode (cc-al) and a layer of the separator (sep), as visualized in Figure 1. The effective density ρ^{eff} is considered to be temperature-independent within the operation temperature range of interest, similar as reported by others [21,55,64,65].

The lamination of the electrode stack matches a network of series and parallel connections of thermal resistors that correspond to the contact resistances at the transition zones of each layer. Hence, anisotropic temperature propagation within the electrode stack is considered by defining the orthotropic effective temperature diffusivity α_{\parallel} parallel (in-plane) and α_{\perp} perpendicular to (through-plane) the direction of the layers:

$$\alpha_{\parallel}(\vartheta) = \sum_{j \in J} \frac{\alpha_j(\vartheta) A_j}{A} \quad (10)$$

$$\alpha_{\perp}(\vartheta) = \frac{L}{\sum_{j \in J} \left(\frac{L_j}{\alpha_j(\vartheta)} \right)} \quad (11)$$

Therein, $\alpha_j : \mathbb{R} \rightarrow \mathbb{R}$ is the j -th materials temperature diffusivity, L_j is the thickness of the j -th stack component, A_j is the electrode surface of the j -th stack component, A is the total electrode surface and L is the total cell sheet thickness [38]. Overall, the effective thermal conductivity matrix k^{eff} within the electrode stack of the three dimensional battery model is defined with respect to the effective stack density ρ^{eff} , heat capacity C_p^{eff} and temperature diffusivities α_{\parallel} and α_{\perp} as follows:

$$k_{\parallel}(\vartheta) = \alpha_{\parallel}(\vartheta) \rho^{eff} C_p^{eff}(\vartheta) \quad (12)$$

$$k_{\perp}(\vartheta) = \alpha_{\perp}(\vartheta) \rho^{eff} C_p^{eff}(\vartheta) \quad (13)$$

$$k^{eff}(\vartheta) = \begin{bmatrix} k_{\perp}(\vartheta) & 0 & 0 \\ 0 & k_{\parallel}(\vartheta) & 0 \\ 0 & 0 & k_{\parallel}(\vartheta) \end{bmatrix} \quad (14)$$

where $k_{\parallel} : \mathbb{R} \rightarrow \mathbb{R}$ is in-plane and $k_{\perp} : \mathbb{R} \rightarrow \mathbb{R}$ is though-plane thermal conductivity.

2.2.6. Coupling of Physics

The governing equations shown in Table A1 in the Appendix A represent the electrochemical behavioral model of the battery. The total heat dissipation density Q_{tot} of the battery with respect to the aforementioned setting is defined in Table A2 in the Appendix A. In Equations (1)–(7), the thermal behavior of the battery and test environment is calculated in dependence of the heat Q dissipated within the electrode stack, while simultaneously exchanging the average of the electrode stack temperature ϑ with the electrochemical model variables of the particle, electrode and electrolyte domains. By Equations (2), (4)–(6), air flow phenomena under temperature dependence are modeled.

3. Results and Discussion

The experimental thermal characterization of the battery cell results is evaluated, discussed and incorporated into the simulation model of the commercially available 40 Ah battery cell. The temperature distribution of the battery cell model is simulated in three scenarios within a test environment. In the first two studies, the thermal model behavior will be analyzed based on the variation of the exterior test conditions of the battery within the climate chamber during controlled external conditions. In the third study, the restrictions and benefits of varying the standard reference cell design with similar internal structure will be evaluated and discussed from a BTMS point of view.

3.1. Geometrical Battery Characterization

A representation of the PHEV battery geometry was created based on details of the materials extracted during the cell disassembly. In Figure 2 the virtual battery cell replication steps are shown:

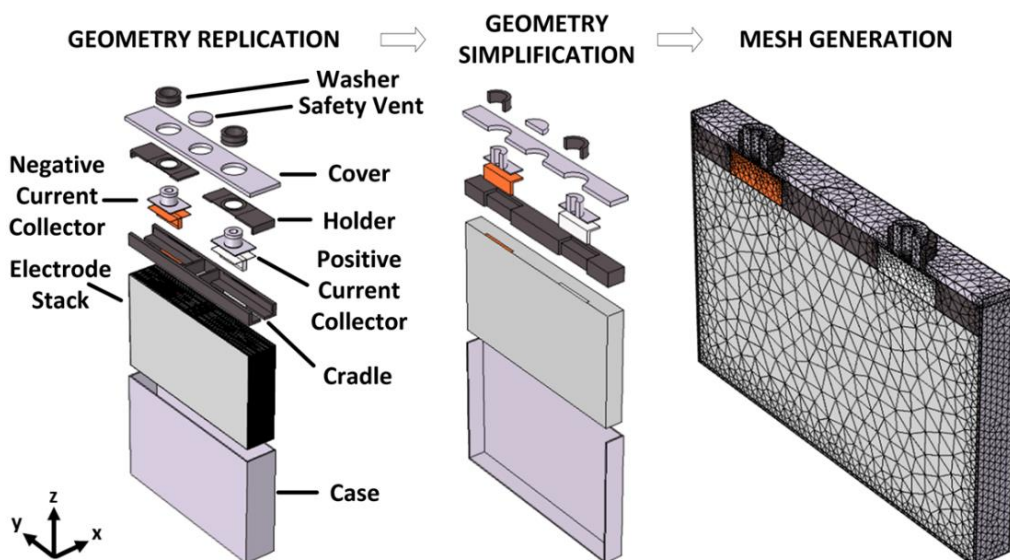


Figure 2. Virtual battery design replication process in three steps.

Geometrical design and material assumptions were made within the battery cell replication process to simplify the model layout. Therefore, redundant fillets and thin shapes are reduced to avoid mesh inaccuracies and excess computational demand. Accordingly, the axial symmetry to the center of the battery cell within the yz -plane is considered. The model's overall battery volume is 185,550 mm³, and the electrode stack sub volume is 143,080 mm³; each a half versus reality.

An analysis of several mesh variations up to an element size of roughly 500,000 elements indicated a negligible influence of the spatial discretization on the resulting temperature distribution within the model when a thermal mesh composed of 63,505 tetrahedral elements with the following quality

quantities is chosen: The average skewness is 0.60 and the minimal skewness is 0.15, while the average condition number is 0.79 and the minimal condition number is 0.26, as presented in Figure 2. The quantity skewness evaluates the anisotropy of angles within mesh elements, whereas the quantity condition number qualifies the matrix isometric transformation properties of the actual elements, in comparison to an ideal tetrahedral element with both equally adjusted angles and maximal condition number. Mesh refinement is considered at areas with more detailed contours like the case and the thinner shapes of the negative and positive current collectors, where high material thermal conductivity exists.

3.2. Characterization Results of Thermal Parameters

The experimental procedures undertaken for this section are explained in Section 2.1.2. The radiation-related surface properties used in Equation (7) of the battery compartments are taken from a material data sheet provided by Optris GmbH® (Berlin, Germany) [66]. The geometry parameters used for the averaging procedures mentioned in Equations (8)–(11) were characterized and reported in our previous study [47]. Altogether, the set of thermal parameters derived for the model parameterization in this study is considered to replicate the battery behavior realistically. The obtained values for the electrode stack components are in good agreement with data reported for a NMC/Graphite type stack in several other studies [17,29,31,32,67]. An overview of the thermal parameters for the electrode stack, the battery and the environment at the 25 °C reference temperature is shown in Table 1:

Table 1. The thermophysical properties of all components at the 25 °C reference temperature.

Material/Meaning	Volume Fraction (%)	Density ρ (kg m^{-3})	Heat Capacity C_p ($\text{J kg}^{-1}\text{K}^{-1}$)	Temperature Diffusivity α (mm^2s^{-1})	Thermal Conductivity k ($\text{W m}^{-1}\text{K}^{-1}$)
Electrode Stack					
Positive Electrode Coating	29.29	4670 [56]	940.00	0.150	0.66
Negative Electrode Coating	25.53	2260 [56]	1040.00	0.615	1.45
Separator	12.90	1009.00	1907.00	0.352	0.68
Aluminum [21]	4.03 * ¹ 0.26 * ²	2700.0.	900.00	84.00	238
Copper [21]	5.37 * ¹ 0.26* ²	8700.00	385.00	111.00	400
Battery					
Electrode Stack	77.12	2650.98	987.55	11.095 * ³ 0.234 * ⁴	29.50 * ³ 0.62 * ⁴
Steel [60]	13.00	8030.00	502.48	4.03	16.27
Synthetic [65] (Acrylic Plastic)	9.36	1190.00	1470.00	0.10	0.18
Environment					
Air [68–70]	-	1.184	1007	21.14	0.026

*¹: Current Collector; *²: Terminal Contact; *³:|| (in-plane); *⁴: \perp (through-plane).

Temperature dependency of the electrode stacks thermal properties had often been assumed to be constants in the temperature range of interest in previous battery modeling approaches [64,65,71]. However, there are several studies that report temperature dependency on material level, and suggest a similar tendency on cell level [30,32,72]. Therefore, the temperature influence on the effective heat capacity and the effective thermal conductivity of the electrode stack is considered for the model parameterization with respect to the temperature range of 20 °C to 80 °C in this study. Finally, fitting

polynomials are derived that will be used to parameterize the thermal properties of the electrode stack in Equation (1).

The experimentally determined stack component's heat capacity and the calculated effective stack variable are shown in Figure 3. The measured values of the heat capacity C_p interval are within $900 \text{ J kg}^{-1}\text{K}^{-1}$ to $1300 \text{ J kg}^{-1}\text{K}^{-1}$ for the electrode coating materials, are within $1200 \text{ J kg}^{-1}\text{K}^{-1}$ to $1900 \text{ J kg}^{-1}\text{K}^{-1}$ for the separator, and are within $900 \text{ J kg}^{-1}\text{K}^{-1}$ to $1200 \text{ J kg}^{-1}\text{K}^{-1}$ for the calculated effective stack heat capacity. The effective stack heat capacity interval is more comparable to the electrode coating's range than to the separator's range. The dominant influence of the electrode coatings is presumably based on the volume ratio within the effective stack capacity. The electrode's coatings are represented by approximately 70%, the separator by 16% and the collector sheets by 14% of the overall stack volume. The value intervals for the different material types are in good agreement with heat capacity measurements in the temperature range up to 50°C at 0% SoC from similar battery cell materials in the literature [29,31]. For each of the measurement objects a least-squares curve fitting procedure is used to analyze the heat capacity trend dependent on the temperature evolution. The resulting curves are nonlinear, and the related coefficient of determination R^2 is above 0.97 in each case. Therefore, it can be concluded that each curve reproduces the temperature dependence seen within the experiments reasonably well. The polynomial orders derived in this study for the different materials, however, remain to be suggestions for the cell under use, since polynomials of orders varying in several degrees are reported in literature [29,72].

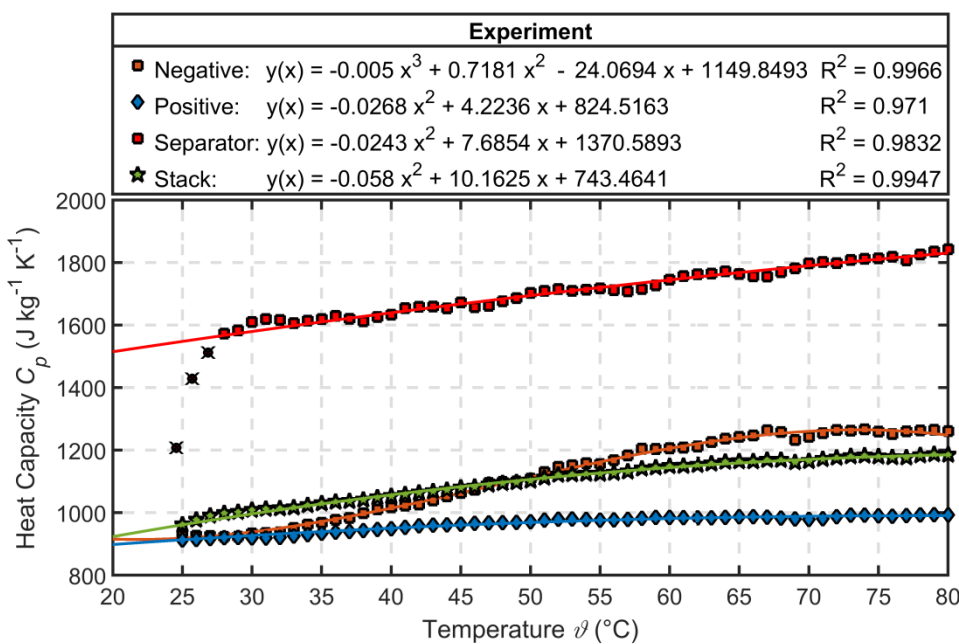


Figure 3. The specific heat capacity C_p of each component of the electrode stack is shown as a function of the temperature ϑ ($^\circ\text{C}$) defined using Differential Scanning Calorimetry (DSC) measurements.

In case of the separator, the experimental values up to 27°C are not considered for the fitting procedure, since such a steep slope is not reported in the literature within the temperature range of interest. Such a physical behavior would be a contrast to the evaluated results of similar separator material reported by others [29]. The measurement error might be attributed to a gap or contact flaw between the separator sample and the crucible bottom, which would lead to an increased heat resistance within the sample system. Therefore, a decrease of the sample system's DSC signal in comparison to the reference system's DSC signal would lead to a decrease of the calculated heat capacity [73].

Additional variable dependencies of heat capacity C_p will be named for completeness, but will not be further considered in this model study. In [29], a nonlinear dependency on SoC is reported for

NMC-type lithium-ion batteries, whereas a similar effect is not seen in iron–phosphate (LFP)-type lithium-ion batteries [72].

In a study by Maleki et al. [31], the influence of ageing on heat capacity is considered, and measurements of fresh and cycled cells, 500 cycles at 45 °C, on cobalt–oxide type battery cells were compared. It was concluded that ageing is negligible in the context of heat capacity in contrast to a study by Vertize et al. [74], where a visible decrease in heat capacity up to 1% at the end of the cell’s lifetime was attributed to the change of internal chemical structures.

The temperature diffusivity of the stack components are considered with respect to the temperature range 20 °C to 80 °C within this study, as shown in Figure 4. The measured sample temperature diffusivity α and the calculated through-plane temperature diffusivity α_{\perp} values are within the interval of $0.1 \text{ mm}^2 \text{s}^{-1}$ to $0.65 \text{ mm}^2 \text{s}^{-1}$, while the in-plane temperature diffusivity α_{\parallel} values are two factors of ten higher within a small interval around $11.1 \text{ mm}^2 \text{s}^{-1}$. A positive linear trend is visible for the separator within the temperature range 20 °C to 80 °C, while the porous material temperature diffusivity shows a negative linear trend.

The in-plane temperature diffusivity α_{\parallel} is based on arithmetic averaging and the through-plane temperature diffusivity α_{\perp} is calculated based on harmonic averaging. Therefore, the rise in magnitude related to the in-plane temperature diffusivity α_{\parallel} is due to the high thermal diffusivity of the current collector sheet materials, while the low values of the through-plane temperature diffusivity α_{\perp} can be related to the short current collector thicknesses and the low magnitudes of the sample material values. For each of the measurement objects, a least-squares curve fitting procedure is considered to analyze the temperature diffusivity trend dependent on the temperature evolution. The resulting curves are linear, and the related coefficients of determination R^2 are within the interval range of 0.75 to 0.98. While the fit for the separator explains the variance of the measurements results less accurately, the fitting curves for the sample materials and the effective values are well matched.

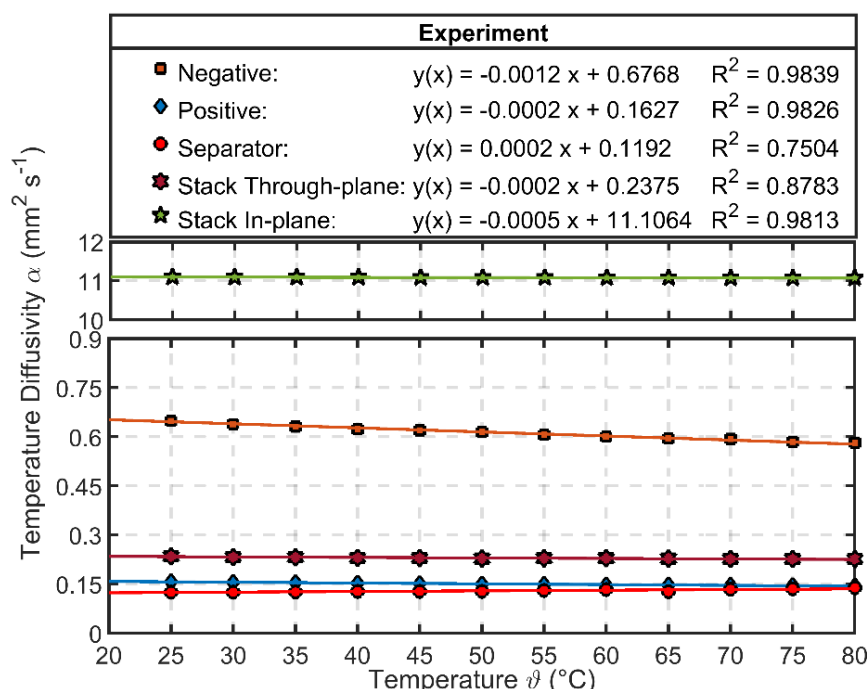


Figure 4. The in-plane α_{\parallel} and through-plane α_{\perp} thermal diffusivity for each electrode stack component is shown as a function of temperature ϑ (°C) obtained from Laser Flash Analysis (LFA) measurements.

Based on equation Equations (12) and (13), the effective thermal conductivity variables are calculated with respect to the previous thermal characterization results. The calculated through-plane thermal conductivity k_{\perp} values are within the interval $0.6 \text{ W m}^{-1} \text{K}^{-1}$ to $0.72 \text{ W m}^{-1} \text{K}^{-1}$, while

the in-plane thermal conductivity k_{\parallel} values are almost two magnitudes higher within the interval $27.5 \text{ W m}^{-1}\text{K}^{-1}$ to $35.0 \text{ W m}^{-1}\text{K}^{-1}$.

In both cases, a nonlinear, positive trend of the effective thermal conductivities is derived. Both quantities of interest increase roughly 15% in magnitude within the temperature range 20°C to 80°C , which is comparable to an increase of C_p of roughly 20% in the same temperature range, while α_{\perp} and α_{\parallel} are decreased by 0.2% and 5%. While the ratio in magnitude of k_{\perp} and k_{\parallel} is clearly induced by α_{\perp} and α_{\parallel} , the positive temperature dependency trend is enhanced by C_p . The heat propagation effect based on the presented results would relate to the following: “Enhanced temperature levels within the electrode stack will lead to increased heat propagation and a decrease of its temperature non-uniformity”. Recent research advances focusing on the enhanced thermal conductivity of electrodes for NMC-type batteries have shown that a positive temperature dependency could be realistic, and even higher thermal conductivity magnitudes can be achieved by innovative electrode designs [33]. The contrary effect, however, was deducted in former studies [32,75] on commercially-available, NMC-type, lithium-ion batteries, which derived twice a decrease in the magnitude of k_{\perp} , and an almost constant k_{\parallel} within the overall temperature range of 0°C to 40°C under the presence of an electrolyte. Therefore, the derived temperature dependency results of the thermal parameters are considered to be trustworthy for the thermal model parameterization of the present study based on the same electrode type, but their transferability to other battery models is limited.

3.3. Thermal Model Study

From a physics point of view, the temperature behavior of a battery cell could be analyzed with a focus on heat dissipation within or heat removal from its encapsulated electrode stack. The battery cells’ temperature distribution is realistically predicted when the balance of the two characteristics is properly matched. While the heat dissipation setting is analyzed and validated for the electrochemical part of the aforementioned battery model in our previous study [47], the present study will further examine the characteristics of heat removal within exterior test settings and realistic battery applications. Three model categories are evaluated in this study with a focus upon the natural convection condition, forced convection condition and the influence of the battery cell design. The underlying cooling type categories and model parameter variations are presented in Figure 5:

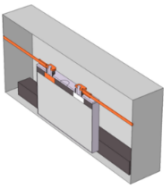
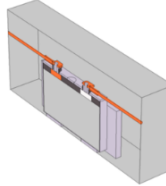
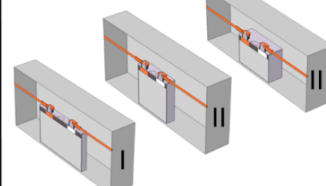
Modeling	Natural Conditions	Forced Conditions	Battery Form Factor
Model-design			
Battery Size (H x L x W, mm ³)	(94,148,26.5)	(94,148,26.5)	I (94, 148, 26.5), II (94, 95, 40.5), III (94, 95, 63.5)
Studytype	Validation	Validation	Simulation
C-rate	0.5, 1.0, 2.0	2.0	2.0
V_{in} (m s ⁻¹)	0.0	0.150, 0.325, 1.000	0.0
ϑ_{ext} (°C)	25.0	22.0	25.0
Coolingtype	Natural Convection	Forced Convection	Isolation, Bottom Cooling (BC), Side Cooling (SC), Face Cooling (FC)

Figure 5. Model study design variants shown with respect to the underlying degrees of freedom.

In the first two model studies, the temperature modeling approach is evaluated in comparison to real case scenarios measured in our laboratory as described in Section 2.1.3.

In the first study, the focus is set on temperature variation dependent on current rates within the battery cell, while an external flow force is considered to be negligible. In the second study the maximal temperature and average heat rejections are analyzed at a constant current rate under varying air inlet velocities V_{in} to match experimentally determined surface temperature patterns of a battery cell located within a test cell array. The test setups are performed to quantify the model accuracy and understand the dynamic of heat generation and heat rejection.

Frequently stated BTMS strategies applied to lithium-ion batteries are bottom cooling (BC), small side cooling (SC) or large face cooling (FC) [29,65]. From the known cooling strategies, a hybrid of high conductive heat pipes with an externally-connected heat removal mechanism is reported to be very effective [3]. A layout of the used cooling concepts is shown in Figure 6:

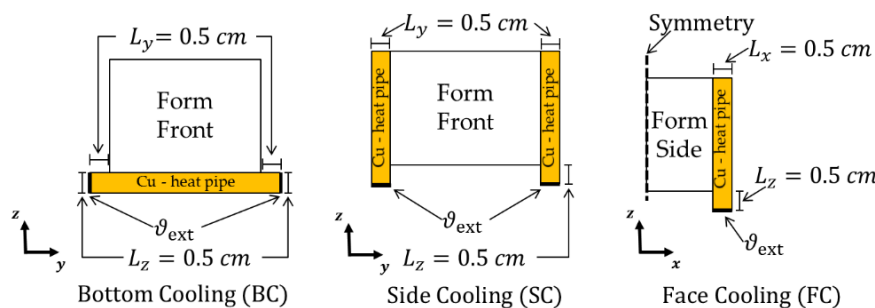


Figure 6. Layout of the conductive cooling concept variations bottom cooling (BC), small side cooling (SC) and large face cooling (FC).

The exterior thermal management might benefit from the known anisotropic thermal conductivity within the electrode stack, when cooling on surfaces next to enhanced heat flux patterns is prioritized. Therefore, model study three aims to evaluate the effectiveness of the proposed cooling concept by evaluating the maximal temperature rise and cooling times until temperature equilibrium is reestablished. The heat removal mechanism is considered to be ideal, which is modeled by a fixed temperature condition ϑ_{ext} on a surface boundary on the heat pipe.

3.3.1. Thermal Validation—Natural and Forced Conditions

For the analysis of the scenario under natural convection, both of the temperature curves during 0.5 C, 1.0 C and 2.0 C during the discharge and charge phase and a subsequent rest phase were taken into account, as shown in Figure 7a,b;

The simulated curves match well for the current levels 0.5 C and 1.0 C with a maximal error below 3.4%; however, at the current level 2.0 C, the error increased up to 7.9%. The absolute difference is comparable to a maximal temperature difference of roughly 0.8 K in the first two cases and a maximal temperature difference up to 2.2 K in the third case.

As a result of the error analysis, the model tends to overestimate the average battery surface temperature at the 2 C current rate, while those lower rates are properly matched. A fluid force dependent on a significant temperature rise, which could present the difference, would be based on the buoyancy effect; an upstream of heated air created under the influence of gravity. Its impact, however, is stated to be negligible when advection is present [8,18].

In the scenario under forced convection the influence of centralized fan air cooling within a climate chamber on the temperature magnitude of the batteries is studied. Therefore, the measured surface temperature curves of three battery cells, which were measured during 2 C cycles, are taken into account. Between each experimental curve a significant deviation of up to a two and a half degree Kelvin temperature difference is observable during the heating phase, each evaluated at the top of the battery. The result proves that the centralized fan is cooling each cell differently based on the position within the test arrangement. Three equivalent air cooling velocities were estimated by matching the

measured surface temperature curves of the batteries within the test arrangement and a simulated average temperature curve of the battery model. All results are shown in Figure 8:

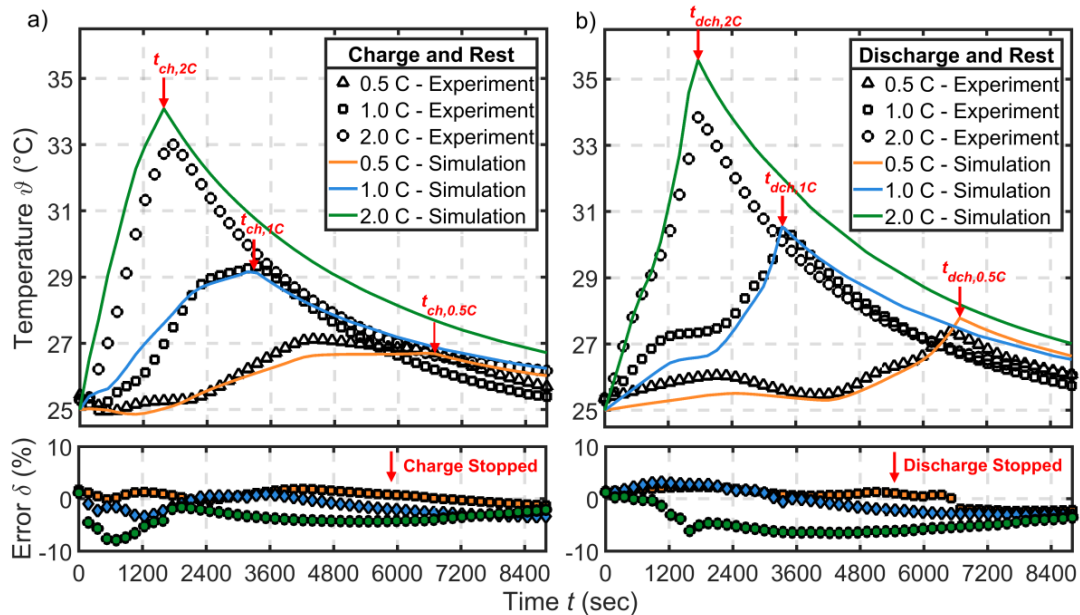


Figure 7. The maximal mean experimental surface temperature ϑ ($^{\circ}\text{C}$), the average simulated surface temperature ϑ ($^{\circ}\text{C}$) and the relative error δ (%) during (a) charge and rest phases and (b) discharge and rest phases dependent on the current rates 0.5 C, 1.0 C and 2.0 C are shown as a function of time t (sec). The ends of the charge times are denoted by t_{ch} and the ends of discharge times are denoted by t_{dch} ; each associated with the corresponding current rate. The reader is referred to Figure 5 for a closer look on the test conditions.

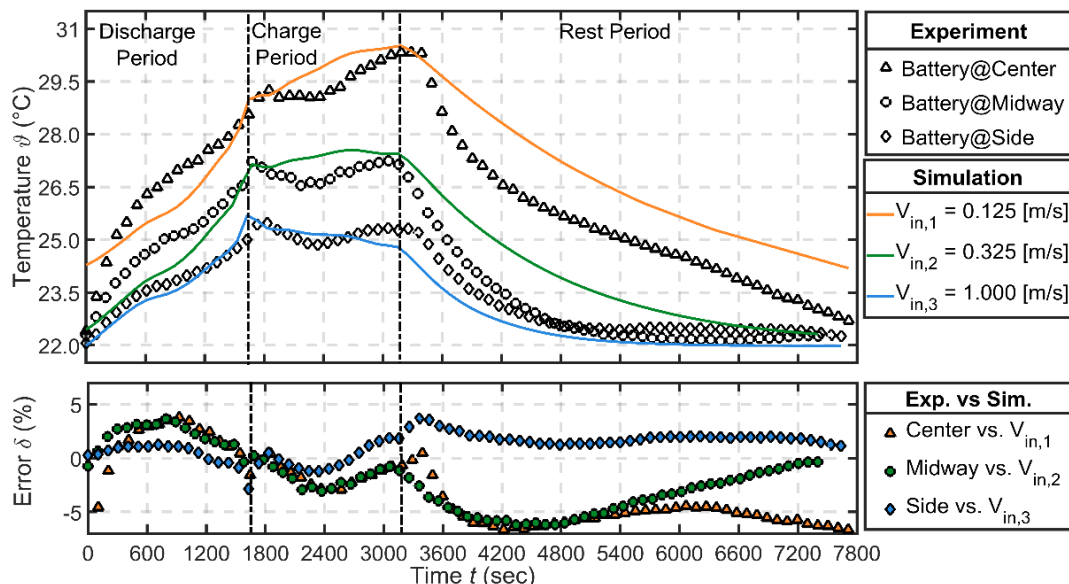


Figure 8. Experimental temperature curves ϑ ($^{\circ}\text{C}$) of three similar battery cells at different locations within the battery test setup, simulated temperature curves ϑ ($^{\circ}\text{C}$) at three different fluid flow inlet magnitudes V_{in} (m s^{-1}) and the relative error δ (%) between experimental and simulated results are shown as a function of time t (sec). The reader is referred to Figure 5 for a closer look on the test conditions.

The simulated curves deviate more pronounced for the batteries corresponding to the center and the midway position with equivalent inlet velocities 0.125 m s^{-1} and 0.325 m s^{-1} with a maximal error below 8.42% at $t = 0 \text{ s}$ and 6.20 % at $t = 4343 \text{ s}$, as compared to the battery at the side with a maximal error below 3.68% at $t = 3462 \text{ s}$ and an equivalent inlet velocity of 1 m s^{-1} . The errors relate to a maximal absolute temperature difference of 1.89 K, 1.44 K and 0.93 K, respectively. While in the first two cases the real battery surface temperature is overestimated, in the last case it is slightly underestimated. Due to the position of the batteries at the center and the middle within the test arrangement, a superimposed cooling influence is visible that is not considered, when only one battery is simulated alone. The superimposed experimental effect could be conductive cooling induced by the highly conductive metal fasteners. The battery at the side that is mostly exposed to fluctuating air is simulated with good accuracy. Hence, the thermal model accuracy increases with increasing equivalent air velocity.

The simulated surface temperature distribution ϑ ($^{\circ}\text{C}$) of the battery cell in both validation cases is shown in Figure 9a,b:

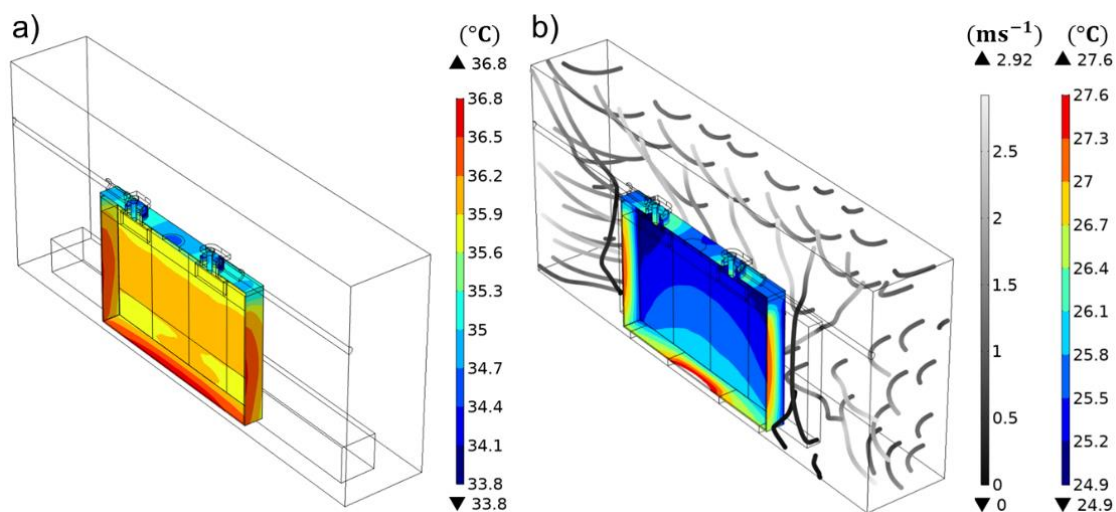


Figure 9. (a) Simulated battery surface temperature distribution ϑ ($^{\circ}\text{C}$) during the natural convection scenario and (b) simulated battery surface temperature distribution ϑ ($^{\circ}\text{C}$) and velocity streamlines at an inlet velocity of $V_{in} = 1 \text{ m s}^{-1}$, both shown at a current rate of 2 C at the end of discharge.

In both cases, the maximal temperature level on the surface is located at the short sides and at the battery cell bottom, which coincides with the direction of in-plane thermal conductivity of the electrode stack. The minimal surface temperature is on the top of the battery cell in both cases, which might be due to presence of the low thermally conducting synthetic cradle on top of the electrode stack. The temperature around the terminal is slightly elevated compared to the rest of the top battery surface, which is due to its direct connection to the electrode stack.

In conclusion of both studies, the model accuracy resembles the realistic match of heat dissipation and heat removal. While heat dissipation increases with the current rate, heat removal is increased with exterior air inlet velocity. During the natural convection scenario, higher deviation occurred, when the temperature increase was more pronounced and heat rejection effects were not fully met within the simulation. During the forced convection scenario, the model accuracy was increased by matching the inlet velocity with the resulting average battery surface temperature during a 2 C cycle. The result at the forced convection scenario supports the suggestion that the temperature deviation between the simulated and experimental results in the natural convection scenario might be induced by the missing buoyancy flow force in the simulation. Altogether, the thermal model is able to predict the spatial temperature behavior of a battery within the test environment under the current rates and airstream velocities of interest with good accuracy.

3.3.2. Model Study—BTMS Compatibility under Battery form Factor Variation

The temperature levels might actually be effectively further decreased compared to the validation scenarios when conductive cooling plates are attached. A direct comparison for the cooling types BC, SC and FC with respect to the form factors I, II and III for the maximal temperature rise $T_{vol,max}(t) = (\text{avg}_{s \in U} \vartheta_{vol}(t, s) - \vartheta_{ext})$ of the electrode stack $U \in \mathbb{R}^3$ is shown in Figure 10:

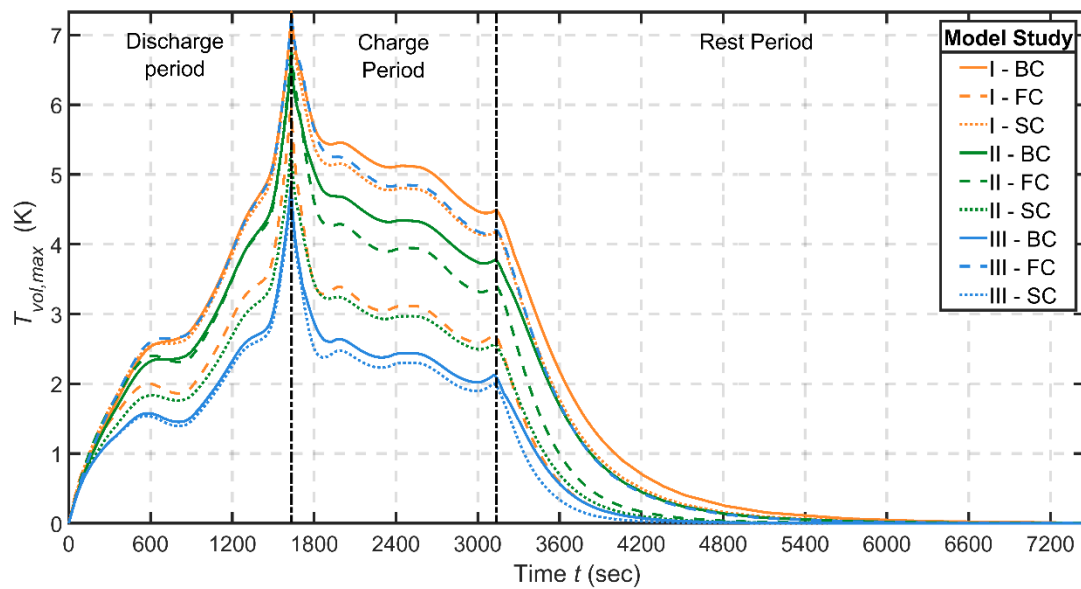


Figure 10. Simulated maximal temperature rise $T_{vol,max}$ in dependence of the cell design and the cooling types BC, SC and FC during a 2 C cycle and 1 hour rest time.

An evaluation of the thermal characteristic within the electrode stack $U \subset \mathbb{R}^3$ is performed based on the following equations:

$$T_{max} = \max_{t \in T} \left(\max_{s \in U} \vartheta_{vol} \right) - \vartheta_{ext} \quad (15)$$

$$\Delta T = \max_{t \in T} \left(\max_{s \in U} \vartheta_{vol} - \min_{s \in U} \vartheta_{vol} \right) \quad (16)$$

$$T_{avg} = \text{avg}_{t \in T_1} \left(\text{avg}_{s \in U} \vartheta_{vol} \right) - \vartheta_{ext} \quad (17)$$

$$\beta = \text{avg}_{t \in T_1} \left(\frac{\max_{s \in U} \vartheta_{vol} - \min_{s \in U} \vartheta_{vol}}{\text{avg}_{s \in U} \vartheta_{vol}} \right) \quad (18)$$

$$\Delta t = t_{\vartheta_{eq}} - t_{cc_{stop}} \quad (19)$$

therein, T_{max} is the maximal temperature rise during the cycle T , ΔT is the maximal spatial temperature difference during the cycle T , T_{avg} is the average temperature rise during the heating phase T_1 , β is the average temperature inhomogeneity indication factor during the heating phase T_1 and Δt is the cooling time until temperature equilibrium is reached after heating is stopped. Each variable is evaluated within the electrode stack volume $U \subset \mathbb{R}^3$ during the denoted test time $t \in T = \{T_1, T_2\}$, where T_1 is the heating phase and T_2 is the rest time.

A rating system compares the results at the 2 C current rate of the standard PHEV2 design I against all other cases. Highlighted color modes and associated thresholds are shown in Table 2. The results for the validation and model study scenarios are shown in Table 3.

Table 2. Rating criteria and associated thresholds for the model study comparison.^{*1}

Significantly Better ^{*2}	Better	Reference	Worse	Significantly Worse ^{*3}
$T_{max} \leq 4.5 \text{ K}$	$T_{max} < 6.1 \text{ K}$	$T_{max} = 6.1 \text{ K}$	$T_{max} > 6.1 \text{ K}$	$T_{max} \geq 7.6 \text{ K}$
$T_{avg} \leq 1.3 \text{ K}$	$T_{avg} < 1.8 \text{ K}$	$T_{avg} = 1.8 \text{ K}$	$T_{avg} > 1.8 \text{ K}$	$T_{avg} \geq 2.3 \text{ K}$
$\Delta T \leq 4.0 \text{ K}$	$\Delta T < 5.4 \text{ K}$	$\Delta T = 5.4 \text{ K}$	$\Delta T > 5.4 \text{ K}$	$\Delta T \geq 6.8 \text{ K}$
$\beta \leq 6.6$	$\beta < 8.8$	$\beta = 8.8$	$\beta > 8.8$	$\beta \geq 11$
$\Delta t \leq 12 : 15$	$\Delta t < 16 : 20$	$\Delta t = 16 : 20$	$\Delta t > 16 : 20$	$\Delta t \geq 20 : 25$

^{*1}: The color code indicates improvement in green types and worsening in red types versus the reference case in yellow. The meanings coincide with the column headings; ^{*2}: 0.75 times reference; ^{*3}: 1.25 times reference.

Table 3. Quantities of interest of the model studies.

Study Type	Model Parameter	$T_{max}(\text{K})$	$T_{avg} (\text{K})$	$\Delta T(\text{K})$	$\beta(\%)$	$\Delta t(\text{mm:ss})$
	C–Rate Phase Velocity Design					
Natural Convection	$\begin{bmatrix} 0.5 \text{ C} & / \\ \text{Charge} & \text{I} \\ 0.5 \text{ C} & / \\ \text{Discharge} & \text{I} \end{bmatrix}$	1.8	0.9	0.1	0.2	>60:00
	$\begin{bmatrix} 1.0 \text{ C} & / \\ \text{Charge} & \text{I} \\ 1.0 \text{ C} & / \\ \text{Discharge} & \text{I} \end{bmatrix}$	4.5	2.5	0.3	0.7	>60:00
	$\begin{bmatrix} 2.0 \text{ C} & / \\ \text{Charge} & \text{I} \\ 2.0 \text{ C} & / \\ \text{Discharge} & \text{I} \end{bmatrix}$	6.2	1.9	0.8	0.8	>60:00
	$\begin{bmatrix} 2.0 \text{ C} & / \\ \text{Charge} & \text{I} \\ 2.0 \text{ C} & / \\ \text{Discharge} & \text{I} \end{bmatrix}$	9.8	5.4	0.8	2.2	>60:00
	$\begin{bmatrix} 2.0 \text{ C} & / \\ \text{Charge} & \text{I} \\ 2.0 \text{ C} & / \\ \text{Discharge} & \text{I} \end{bmatrix}$	12.2	4.4	1.7	2.0	>60:00
	$\begin{bmatrix} 2.0 \text{ C} & 0.125 \\ \text{Cycle} & \text{I} \\ 2.0 \text{ C} & 0.325 \\ \text{Cycle} & \text{I} \\ 2.0 \text{ C} & 1.000 \\ \text{Cycle} & \text{I} \end{bmatrix}$	10.0	6.3	3.4	4.7	>60:00
Forced Convection	$\begin{bmatrix} 2.0 \text{ C} & 0.125 \\ \text{Cycle} & \text{I} \\ 2.0 \text{ C} & 0.325 \\ \text{Cycle} & \text{I} \\ 2.0 \text{ C} & 1.000 \\ \text{Cycle} & \text{I} \end{bmatrix}$	8.3	4.2	3.7	5.9	>60:00
	$\begin{bmatrix} 2.0 \text{ C} & / \\ \text{Cycle} & \text{I} \\ 2.0 \text{ C} & / \\ \text{Cycle} & \text{II} \\ 2.0 \text{ C} & / \\ \text{Cycle} & \text{III} \end{bmatrix}$	7.2	2.9	4.2	7.2	26:44
	$\begin{bmatrix} 2.0 \text{ C} & / \\ \text{Cycle} & \text{I} \\ 2.0 \text{ C} & / \\ \text{Cycle} & \text{II} \\ 2.0 \text{ C} & / \\ \text{Cycle} & \text{III} \end{bmatrix}$	6.1	1.8	5.4	8.8	16:20
	$\begin{bmatrix} 2.0 \text{ C} & / \\ \text{Cycle} & \text{I} \\ 2.0 \text{ C} & / \\ \text{Cycle} & \text{II} \\ 2.0 \text{ C} & / \\ \text{Cycle} & \text{III} \end{bmatrix}$	6.8	2.4	6.1	10.7	21:00
Conduction–Face –	$\begin{bmatrix} 2.0 \text{ C} & / \\ \text{Cycle} & \text{I} \\ 2.0 \text{ C} & / \\ \text{Cycle} & \text{II} \\ 2.0 \text{ C} & / \\ \text{Cycle} & \text{III} \end{bmatrix}$	7.3	3.0	6.6	12.6	30:20
	$\begin{bmatrix} 2.0 \text{ C} & / \\ \text{Cycle} & \text{I} \\ 2.0 \text{ C} & / \\ \text{Cycle} & \text{II} \\ 2.0 \text{ C} & / \\ \text{Cycle} & \text{III} \end{bmatrix}$	7.3	3.1	6.4	11.9	31:17
	$\begin{bmatrix} 2.0 \text{ C} & / \\ \text{Cycle} & \text{I} \\ 2.0 \text{ C} & / \\ \text{Cycle} & \text{II} \\ 2.0 \text{ C} & / \\ \text{Cycle} & \text{III} \end{bmatrix}$	5.4	2.1	4.4	7.8	18:12
	$\begin{bmatrix} 2.0 \text{ C} & / \\ \text{Cycle} & \text{I} \\ 2.0 \text{ C} & / \\ \text{Cycle} & \text{II} \\ 2.0 \text{ C} & / \\ \text{Cycle} & \text{III} \end{bmatrix}$	4.7	1.6	3.8	6.1	12:45
Conduction–Bottom –	$\begin{bmatrix} 2.0 \text{ C} & / \\ \text{Cycle} & \text{I} \\ 2.0 \text{ C} & / \\ \text{Cycle} & \text{II} \\ 2.0 \text{ C} & / \\ \text{Cycle} & \text{III} \end{bmatrix}$	7.3	3.1	6.4	12.4	39:09
	$\begin{bmatrix} 2.0 \text{ C} & / \\ \text{Cycle} & \text{I} \\ 2.0 \text{ C} & / \\ \text{Cycle} & \text{II} \\ 2.0 \text{ C} & / \\ \text{Cycle} & \text{III} \end{bmatrix}$	6.7	2.6	5.8	11.1	31:09
	$\begin{bmatrix} 2.0 \text{ C} & / \\ \text{Cycle} & \text{I} \\ 2.0 \text{ C} & / \\ \text{Cycle} & \text{II} \\ 2.0 \text{ C} & / \\ \text{Cycle} & \text{III} \end{bmatrix}$	4.8	1.7	3.9	6.6	16:29
	$\begin{bmatrix} 2.0 \text{ C} & / \\ \text{Discharge} & \text{I} \\ 2.0 \text{ C} & / \\ \text{Discharge} & \text{II} \\ 2.0 \text{ C} & / \\ \text{Discharge} & \text{III} \end{bmatrix}$	14.7	5.7	1.5	1.7	/
Isolation	$\begin{bmatrix} 2.0 \text{ C} & / \\ \text{Discharge} & \text{I} \\ 2.0 \text{ C} & / \\ \text{Discharge} & \text{II} \\ 2.0 \text{ C} & / \\ \text{Discharge} & \text{III} \end{bmatrix}$	15.0	5.8	1.6	1.9	/
	$\begin{bmatrix} 2.0 \text{ C} & / \\ \text{Discharge} & \text{I} \\ 2.0 \text{ C} & / \\ \text{Discharge} & \text{II} \\ 2.0 \text{ C} & / \\ \text{Discharge} & \text{III} \end{bmatrix}$	14.4	5.5	1.4	1.7	/

The best case scenario for each quantity of interest is given at cell design III/SC and III/BC. The worst case scenario for each quantity of interest is given at III/FC, I/SC and I/BC. The difference between the best and worst case to remove heat gradually increases from design I over II to III. Therefore, a BTMS could maintain an improved battery temperature performance at design III, especially with a

strategy based on SC. However, if SC and BC are not applicable, a significant performance reduction is expected to occur in comparison with the best reference case I/FC.

During the natural convection, forced convection and isolation case at 2 °C, higher temperature levels were reached than within each case with dominant cooling by conduction. From isolation, over natural convection to the forced convection case, the maximal and average temperature rise gradually decreases, while the maximal temperature difference and average temperature inhomogeneity indication factor gradually increase. The inverse proportionality of the two subcategories: “Temperature magnitude and temperature inhomogeneity” is reported in other studies [55,76] as well. This is deemed to be a challenge for an appropriate BTMS design.

Work at National Renewable Energy Laboratory was conducted to develop ageing models of lithium-ion cells that consider the impact of temperature and charge/discharge cycles on battery lifetime. The study [7] by Smith et al. on an NMC/Graphite chemistry type battery cell reported on the influence of the battery cell’s yearly average temperature on the battery life. Within an average depth of discharge (DOD) range in between 20% to 75% for an average battery temperature of 20 °C, a lifetime of roughly ten years, and for an average battery temperature of 33 °C, a lifetime of approximately five years, was stated [7]. The difference in 13 K average battery temperature equals a lifetime difference of roughly five years [19], which likewise equals a lifetime difference of four to five months per degree Kelvin. Hence, from the evaluated cases in the present model study, the highest average temperature increase in each cell design combined with isolation would be comparable to a lifetime reduction of roughly two years. Similarly, each battery in scenario I/FC, III/SC or III/BC would equally benefit by the appropriately chosen BTMS cooling with a maximal lifetime enhancement of seven to eight months; a difference up to one year and four to five months.

4. Conclusions

The developed electrochemical–thermal battery model allows simulations of the spatial–thermal behavior of a commercial lithium–ion battery cell under realistic environmental conditions with good accuracy, and is a trustworthy tool to investigate the correlation between the system layout and the thermal characteristic of the incorporated battery type.

Within validation scenarios, the influence of convection-induced cooling at a commercially available PHEV2 format lithium ion battery was analyzed under different current rates and fan airstream velocities. Heat removal by forced convection is an effective choice to decrease the temperature of the battery cell based on controlled air velocity. The maximal relative error of the model depends on the current rate and the airstream inlet velocity. During natural convection the maximal relative model deviation at the end of discharge increased from 3.4% to 7.8% with an increasing current rate. However, forced convection with increasing airstream velocity decreased the model deviations from 8.2% to 3.68%. Therefore, we conclude that the increased model deviation at a high current rate during natural convection is rather due to missing heat removal phenomena, which are not captured by the thermal battery model, than to a model error related to heat generation. From a modeling practice point of view, an improvement of the model results at natural convection is expected when the physics of a buoyancy flow is considered.

Conductive cooling strategies are even more reliable than convective cooling strategies when the internal battery structure is considered. The work shows that preferential heat rejection patterns within the battery cell geometry can effectively be used within a BTMS cooling strategy to reduce the impact of temperature on the battery cell life. A comparison of the worst and best case situations for heat removal from batteries of similar thermal characteristics has shown that the use of a properly designed BTMS relates to a battery lifespan enhancement of almost one and a half years, when the battery is cycled within an application with average demand at a 2 °C current rate and room temperature conditions. A parallel improvement in temperature magnitude and temperature homogeneity was realized with a battery form factor change from the PHEV2 format to the design variants II or III at a BTMS conductive cooling strategy with SC or BC, instead of FC.

The results show that the electrochemical–thermal model with the derived set of parameters is able to make adequate quantitative predictions about the thermal state of the battery during cycling. Furthermore, it can be used to draw conclusions about the performance of the batteries in arbitrary cell and system designs.

Author Contributions: Conceptualization, G.L., S.G., F.S., and C.A.; Data curation, G.L., O.Z. and U.K.; Formal analysis, G.L.; Funding acquisition, F.S.; Investigation, G.L., O.Z. and U.K.; Methodology, G.L., O.Z. and S.G.; Project administration, U.K.; Resources, U.K. and F.S.; Software, G.L. and O.Z.; Supervision, C.A.; Validation, G.L. and O.Z.; Visualization, G.L. and O.Z.; Writing—Original draft, G.L.; Writing—Review and editing, U.K., S.G., F.S. and C.A. All authors have read and agreed to the published version of the manuscript.

Funding: This research “BaSyMo” (FKZ: 03ET6087I) was funded by the Federal Ministry of Economic Affairs and Energy (BMWi).

Acknowledgments: The authors gratefully acknowledge the financial support provided by BMWi, the German Federal Ministry of Economic Affairs and Energy, for funding of the project BaSyMo (FKZ: 03ET6087I). We like to thank our project partner for their excellent collaboration on the topic of battery research: ElringKlinger AG.

Conflicts of Interest: The authors declare no conflict of interest. The founding sponsors had no role in the design of the study; in the collection, analysis, or interpretation of data; in the writing of the manuscript, and in the decision to publish the results.

Appendix A

The derivation and discussions of the model type [77–79] and the implementation in COMSOL Multiphysics® [65] can be found within the reference list. For details on the model parameterization, the reader is referred to the study [47] by Liebig et al. The governing equations are shown Table A1. Parameter modifications with respect to the underlying modifications are denoted by $(\cdot)_{eff}$. Phase and domain indices are denoted by l , s and $k = \{ne, pe, sep\}$, respectively:

Table A1. The governing equations of the physicochemical model.

Domain/Meaning	Governing Equation	Boundary Condition
Solid Phase/Electrodes		
Mass Conservation	$\frac{\partial c_{s,k}}{\partial t} = \frac{1}{r_k^2} \frac{\partial}{\partial r} \left(D_{s,k}^{eff} r_k^2 \frac{\partial c_{s,k}}{\partial r} \right)$	$\frac{\partial c_{s,k}}{\partial r} \Big _{r=0} = 0; D_{s,k}^{eff} \frac{\partial c_{s,k}}{\partial r} \Big _{r=r_k} = -\frac{j_k^{eff}}{a_k F}$
Charge Conservation	$\frac{\partial}{\partial \delta} \left(\sigma_{s,k}^{eff} \frac{\partial \phi_{s,k}}{\partial \delta} \right) = j_k^{eff}$	$\frac{\partial \phi_{s,neg}}{\partial x} \Big _{x=L_{neg}} = \frac{\partial \phi_{s,pos}}{\partial x} \Big _{x=L_{neg}+L_{sep}} = 0$ $-\sigma_{s,neg}^{eff} \frac{\partial \phi_{s,neg}}{\partial \delta} \Big _{\delta=0} = \sigma_{s,pos}^{eff} \frac{\partial \phi_{s,pos}}{\partial \delta} \Big _{\delta=L} = \frac{I}{A}$
Liquid-Phase/Electrolyte		
Mass Conservation	$\epsilon_{l,k} \frac{\partial c_{l,k}}{\partial t} = \frac{\partial}{\partial \delta} \left(D_{l,k}^{eff} \frac{\partial c_{l,k}}{\partial \delta} \right) + \frac{1-t_0^+}{F} j_k^{eff}$	$\frac{\partial c_{l,neg}}{\partial x} \Big _{\delta=0} = \frac{\partial c_{l,pos}}{\partial x} \Big _{\delta=L} = 0$
Charge Conservation	$\frac{\partial}{\partial \delta} \left(\sigma_{l,k}^{eff} \frac{\partial \phi_{s,k}}{\partial \delta} \right) - \frac{\partial}{\partial \delta} \left(\sigma_{D,k}^{eff} \frac{\partial \ln c_{l,k}}{\partial \delta} \right) = -j_k^{eff}$	$\frac{\partial \phi_{l,neg}}{\partial x} \Big _{\delta=0} = \frac{\partial \phi_{l,pos}}{\partial x} \Big _{\delta=L} = 0$
Reaction Kinetics		
Reaction Rate Pore Wall Flux	$j_k^{ref} = a_k K_k \left(c_{s,k}^{max} - c_{s,k}^{surf} \right)^{1-\alpha} \left(c_{s,k}^{surf} \right)^\alpha \left(\frac{c_{l,k}}{c_{l,ref}} \right)^{1-\alpha} \left[e^{\left(\frac{(1-\alpha)F\mu_k}{RT} \right)} - e^{\left(\frac{-\alpha F\mu_k}{RT} \right)} \right]$	
Over-Potential	$\mu_k = \phi_{s,k} - \phi_{l,k} - U_k(SoC_k); SoC_k = \frac{c_{s,k}^{surf}}{c_{s,k}^{max}}$	
Electrode Stack		
Terminal Voltage	$V_{cell} = \phi_{s,pos}(\delta = L) - \phi_{s,neg}(\delta = 0) + \frac{I R_0}{A}$	

Based on the solution variables, the heat dissipation sources will be quantified. The total battery heat dissipation density Q_{tot} is implemented in this study as the sum of the integrated heat dissipation

sources resulting during the energy transfer processes [27]. Heat by side reactions and particle mixing within the electrode domains is considered negligible [17,80]. The heat dissipation density variable definitions are shown in Table A2:

Table A2. The heat dissipation sources within the physicochemical model.

Domain/meaning	Equation
Electrode ($k = \text{ne, pe}$)	
Reversible Heat	$Q_{rev,k} = j_k^{\text{eff}} T \frac{\partial U_k^{\text{avg}}}{\partial T}$
Irreversible Polarization Heat	$Q_{irr,pol,k} = j_k^{\text{eff}} \mu_k$
Irreversible Ohmic Heat	$Q_{irr,ohmic,k} = \sigma_{s,k}^{\text{eff}} \left(\frac{\partial \phi_{s,k}}{\partial \delta} \right)^2 + \sigma_{l,k}^{\text{eff}} \left(\frac{\partial \phi_{l,k}}{\partial \delta} \right)^2 + \sigma_{D,k}^{\text{eff}} \frac{\partial \ln c_{l,k}}{\partial \delta} \frac{\partial \phi_{l,k}}{\partial \delta}$
Separator ($k = \text{sep}$)	
Irreversible Ohmic Heat	$Q_{irr,ohmic,k} = \sigma_{l,k}^{\text{eff}} \left(\frac{\partial \phi_{l,k}}{\partial \delta} \right)^2 + \sigma_{D,k}^{\text{eff}} \frac{\partial \ln c_{l,k}}{\partial \delta} \frac{\partial \phi_{l,k}}{\partial \delta}$
Terminal/Current Collector ($k = 0$)	
Irreversible Ohmic Heat	$Q_{irr,ohmic,0} = \frac{l^2 R_0}{A}$
Electrode Stack	
Total Heat Dissipation	$Q_{tot} = \sum_k \left(\int_0^{L_k} Q_{rev,k} + Q_{irr,pol,k} + Q_{irr,ohmic,k} dx \right) + Q_{irr,ohmic,0}$

The upcoming set of equations is chosen and partially refined to reproduce the electrode balancing and reaction kinetics of the cell with respect to the governing equations and underlying domains $k = \text{ne, pe, sep}$ defined in Table A1:

- The inactive fraction of the electrodes' SoC windows is calculated by:

$$f_k = 1 - (SoC_k^{\max} - SoC_k^{\min}) \quad (\text{A1})$$

- The actual electrode capacities Q_{neg} and Q_{pos} are calculated based on the fact that the usable capacity Q_{cell} represents the active material loading, while the counterparts in each electrode remain inactive:

$$Q_k = \frac{Q_{cell}}{(1 - f_k)} \quad (\text{A2})$$

- The theoretical electrode capacities are calculated as follows:

$$Q_k^{\text{theo}} = \frac{\rho_k \cdot V_k \cdot F}{M_k} \quad (\text{A3})$$

- The electrodes' active material fraction is received by calculating the ratio of the actual electrode capacity of the theoretical electrode capacity:

$$\epsilon_{s,k} = \frac{Q_k}{Q_k^{\text{theo}}} \quad (\text{A4})$$

- The specific surface area is calculated as follows:

$$a_k = \frac{3 \cdot \epsilon_{s,k}}{r_k} \quad (\text{A5})$$

- Similarly the actual surface area is calculated as follows:

$$S_k = \frac{3 \cdot V_k \cdot \epsilon_{s,k}}{r_k} \quad (\text{A6})$$

- The temperature dependence of model variables is considered by applying the Arrhenius relation:

$$n(T) = n_{ref} \cdot e^{\frac{E_n^{act}}{R} \left(\frac{1}{T_{ref}} - \frac{1}{T} \right)} \quad (\text{A7})$$

where n is the variable, n_{ref} is the variables value at the reference temperature T_{ref} , E_n^{act} is the activation energy, R is the universal gas constant and T is the temperature variable.

- Each electrode's exchange current density is defined as temperature-dependent with respect to [56]:

$$j_k^{eff}(c_{l,k}, c_{s,k}, T) = j_k^{ref}(c_{l,k}, c_{s,k}) \cdot e^{\frac{E_{j_k}^{act}}{R} \left(\frac{1}{T_{ref}} - \frac{1}{T} \right)} \quad (\text{A8})$$

- Each electrode's diffusion coefficient is dependent upon the electrodes SoC and temperature. Therefore, the following equations are defined with respect to [56]:

$$D_{s,k}^{eff}(SoC, T) = D_{s,k}^{ref}(SoC) \cdot e^{\frac{E_{D_{s,k}}^{act}}{R} \left(\frac{1}{T_{ref}} - \frac{1}{T} \right)} \quad (\text{A9})$$

where

$$\log_{10} D_{s,neg}^{ref}(SoC) \left(\frac{cm^2}{s} \right) = \begin{cases} -3.5 \cdot SoC - 8.8 & 0 < SoC < 0.2 \\ 59.375 \cdot SoC^3 - 26.563 \cdot SoC^2 - 8.9125 & 0.2 < SoC < 0.3 \\ -9.7 & 0.3 < SoC < 1.0 \end{cases} \quad (\text{A10})$$

and

$$\log_{10} D_{s,pos}^{ref}(SoC) \left(\frac{cm^2}{s} \right) = -1.682 \cdot SoC - 9.127 \quad (\text{A11})$$

- The electrolyte diffusion coefficient is defined as follows, as is taken from Nyman et al. [81]:

$$D_{l,k}^{eff}(c_{l,k}, T) \left(\frac{m^2}{s} \right) = D_{l,k}^{ref}(c_{l,k}) \cdot \epsilon_{l,k}^\beta \cdot e^{\frac{E_{D_{l,k}}^{act}}{R} \left(\frac{1}{T_{ref}} - \frac{1}{T} \right)} \quad (\text{A12})$$

where

$$D_{l,k}^{ref}(c_{l,k}) = 8.794 \cdot 10^{-11} c_{l,k}^2 - 3.972 \cdot 10^{-10} c_{l,k} + 4.862 \cdot 10^{-10} \quad (\text{A13})$$

- The Li^+ transference number t_0^+ is defined as follows, as taken from Nyman et al. [81]:

$$t_0^+(c_{l,k}) = -0.1287 \cdot c_{l,k}^3 + 0.4106 \cdot c_{l,k}^2 - 0.4717 \cdot c_{l,k} + 0.4492 \quad (\text{A14})$$

- The effective thermodynamic activity f_{cl}^{eff} coefficient is defined as follows, as taken from [81]:

$$\begin{aligned} f_{cl}^{eff}(c_{l,k}, T) &= \left(1 + \frac{\partial \ln(f_{cl})}{\partial \ln(c_{l,k})} \right)(c_{l,k}, T) \\ &= \frac{0.28687 \cdot c_{l,k}^2 - 0.74678 \cdot c_{l,k} + 0.44103}{(1-t_0^+(c_{l,k}))} \cdot e^{\frac{E_{f_{cl}}^{act}}{R} \left(\frac{1}{T_{ref}} - \frac{1}{T} \right)} \end{aligned} \quad (\text{A15})$$

- The electrolyte conductivity is defined as follows, as taken from Zavalis et al. [82]:

$$\sigma_{l,k}^{eff}(c_{l,k}, T) \left(\frac{S}{m} \right) = \sigma_{l,k}^{ref}(c_{l,k}) \cdot \epsilon_{l,k}^{\beta} \cdot e^{\frac{E_{o,l,k}^{Act}}{R} \left(\frac{1}{T_{ref}} - \frac{1}{T} \right)} \quad (\text{A16})$$

where

$$\sigma_{l,k}^{ref}(c_{l,k}) = 0.1297 \cdot c_{l,k}^2 - 2.51 \cdot c_{l,k}^{1.5} - 0.3329 \cdot c_{l,k} \quad (\text{A17})$$

- The effective electrode conductivity is defined as follows:

$$\sigma_{s,k}^{eff} = \sigma_{s,k}^{ref} \cdot \epsilon_{l,k} \quad (\text{A18})$$

- The effective diffusional electrolyte conductivity is defined as follows:

$$\sigma_{D,k}^{eff}(c_{l,k}, T) \left(\frac{S}{m} \right) = \frac{2\sigma_{l,k}^{eff}(c_{l,k}, T)RT}{F} \cdot f_{cl}^{eff}(c_{l,k}, T) \cdot (1 - t_0^+(c_{l,k})) \quad (\text{A19})$$

Table A3. Summary of the all material and cell properties resembling the analyzed battery cell.

Meaning	Symbol	Unit	Negative Electrode	Separator	Positive Electrode	Reference
Design Specifications						
Domain Thickness	L	(μm)	47.5	24.7	54.5	[47]
Electrode Plate Area	A	(m^2)		2.1024		[47]
Particle Radius	r	(μm)	9.89		1.72	[47]
Actual Capacity	Q	(Ah)	48.17		69.20	(A2)
Active Electrode Volume	V	(cm^3)	99.86		114.58	[47]
Molar Mass	M	(g mol^{-1})	72.0		96.5	[56]
Density	ρ	(kg m^{-3})	2260 [83]		4670 [84]	[56]
Theoretical Capacity	Q^{theo}	(Ah)	84.01		148.61	(A3)
Lower Electrode SoC	SoC^{min}		0.01		0.415	[47]
Upper Electrode SoC	SoC^{max}		0.785		0.955	[47]
Active Material Fraction	ϵ_s		0.548		0.457	(A4)
Specific Surface Area	a	(m^{-1})	172,730		825880	(A5)
Surface Area	S	(m^2)	17.25		94.63	(A6)
Electrolyte Volume Fraction	ϵ_l		0.308	0.395 [56]	0.191	[47,56]
Inactive Volume Fraction	f		0.189		0.45	(A1)
Kinetic and Transport Properties						
Open-Circuit Potential	U	(V)	Taken from [47]		Taken from [56]	[47,56]
Temperature derivative of Open-Circuit Potential	$\frac{dU}{dT}$	(V K^{-1})	Taken from [27]		$-7.255 \cdot 10^{-5}$ [26]	[26,27]
Charge Transfer Symmetry Factor	α		0.5		0.5	[53]

Table A3. *Cont.*

Meaning	Symbol	Unit	Negative Electrode	Separator	Positive Electrode	Reference
Maximum Lithium Intercalation Concentration	c_s^{max}	(mol m ⁻³)	31389		48396	[56]
Equilibrium Electrolyte Concentration	$c_{l,ini}$	(mol m ⁻³)		1000		[56]
cmidrule1-7 Effective Electrode Diffusion Coefficient	D_s^{eff}	(m ² s ⁻¹)	(A9)		(A9)	[56]
Reference Electrode Diffusion Coefficient	D_s^{ref}	(m ² s ⁻¹)	(A10)		(A11)	[56]
Effective Electrode Electronic Conductivity	σ_s^{eff}	(s m ⁻¹)	(A18)		(A18)	[56]
Reference Electrode Electronic Conductivity	σ_s^{ref}	(s m ⁻¹)	100		10	[56]
Effective Electrolyte Conductivity	σ_l^{ref}	(s m ⁻¹)		(A16)		[81]
Reference Electrolyte Conductivity	σ_l^{ref}	(s m ⁻¹)		(A17)		[81]
Bruggeman Exponent	β		1.5	1.5	1.5	[85]
Effective Diffusional Electrolyte conductivity	σ_D^{eff}	(s m ⁻¹)		(A19)		[60]
Effective Electrolyte Diffusion Coefficient	D_l^{eff}	(m ² s ⁻¹)		(A12)		[81,82]
Reference Electrolyte Diffusion Coefficient	D_l^{ref}	(m ² s ⁻¹)		(A13)		[81]
Li-transference Number	t_0^+			(A14)		[81]
Effective Electrolyte Activity coefficient	f_{cl}^{eff}			(A15)		[81,82]
Reaction Rate Coefficient	K_k	(m ^{2.5} mol ^{-0.5} s ⁻¹)	2.41 · 10 ⁻⁵		2.41 · 10 ⁻⁵	[47]
Double Layer Capacitance	C_{dl}	(F m ⁻²)	5.18		0.96	[47]
Ohmic Resistance	R_0	(mΩ)		1.24		[47]
Exchange Current Density Activation Energy	E_j^{act}	(kJmol ⁻¹)	48.9		78.1	[56]
Electrode Diffusion Activation Energy	$E_{D_s}^{act}$	(kJmol ⁻¹)	28.8		49.6	[56]
Electrolyte Diffusion Activation Energy	$E_{D_l}^{act}$	(kJmol ⁻¹)		16.5		[82]
Electrolyte Conductivity Activation Energy	$E_{\sigma_l}^{act}$	(kJmol ⁻¹)		4.0		[82]
Electrolyte Activity Coefficient	$E_{f_{cl}}^{act}$	(kJmol ⁻¹)		-1.0		[82]

References

- Arora, S. Selection of thermal management system for modular battery packs of electric vehicles: A review of existing and emerging technologies. *J. Power Sources* **2018**, *400*, 621–640. [CrossRef]
- Khan, M.; Swierczynski, M.; Kær, S. Towards an ultimate battery thermal management system: A review. *Batteries* **2017**, *3*, 9. [CrossRef]

3. Zhao, R.; Zhang, S.; Liu, J.; Gu, J. A review of thermal performance improving methods of lithium ion battery: Electrode modification and thermal management system. *J. Power Sources* **2015**, *299*, 557–577. [[CrossRef](#)]
4. Waldmann, T.; Wilka, M.; Kasper, M.; Fleischhammer, M.; Wohlfahrt-Mehrens, M. Temperature dependent ageing mechanisms in Lithium-ion batteries—A Post-Mortem study. *J. Power Sources* **2014**, *262*, 129–135. [[CrossRef](#)]
5. Barré, A.; Deguilhem, B.; Grolleau, S.; Gérard, M.; Suard, F.; Riu, D. A review on lithium-ion battery ageing mechanisms and estimations for automotive applications. *J. Power Sources* **2013**, *241*, 680–689. [[CrossRef](#)]
6. Ma, S.; Jiang, M.; Tao, P.; Song, C.; Wu, J.; Wang, J.; Deng, T.; Shang, W. Temperature effect and thermal impact in lithium-ion batteries: A review. *Prog. Nat. Sci. Mater. Int.* **2018**, *28*, 653–666. [[CrossRef](#)]
7. Smith, K.; Shi, Y.; Wood, E.; Pesaran, A. Advanced automotive battery conference, Detroit, Michigan. In *Presentation: Optimizing Battery Usage and Management for Long Life*; National Renewable Energy Laboratory: Golden, CO, USA, 2016.
8. Ye, B.; Rubel, M.; Li, H. Design and optimization of cooling plate for battery module of an electric vehicle. *Appl. Sci.* **2019**, *9*, 754. [[CrossRef](#)]
9. Liu, L.; Park, J.; Lin, X.; Sastry, A.M.; Lu, W. A thermal-electrochemical model that gives spatial-dependent growth of solid electrolyte interphase in a Li-ion battery. *J. Power Sources* **2014**, *268*, 482–490. [[CrossRef](#)]
10. Liu, L.; Zhu, M. Modeling of SEI layer growth and electrochemical impedance spectroscopy response using a thermal-electrochemical model of Li-ion batteries. *ECS Trans.* **2014**, *61*, 43–61. [[CrossRef](#)]
11. Bizeray, A.M.; Zhao, S.; Duncan, S.R.; Howey, D.A. Lithium-ion battery thermal-electrochemical model-based state estimation using orthogonal collocation and a modified extended Kalman filter. *J. Power Sources* **2015**, *296*, 400–412. [[CrossRef](#)]
12. Behrou, R.; Maute, K. Numerical modeling of damage evolution phenomenon in solid-state lithium-ion batteries. *J. Electrochem. Soc.* **2017**, *164*, 2573–2589. [[CrossRef](#)]
13. Cai, L.; White, R.E. Mathematical modeling of a lithium ion battery with thermal effects in COMSOL Inc. Multiphysics (MP) software. *J. Power Sources* **2011**, *196*, 5985–5989. [[CrossRef](#)]
14. Jalkanen, K.; Aho, T.; Vuorilehto, K. Entropy change effects on the thermal behavior of a LiFePO₄/graphite lithium-ion cell at different states of charge. *J. Power Sources* **2013**, *243*, 354–360. [[CrossRef](#)]
15. Capron, O.; Jaguemont, J.; Gopalakrishnan, R.; Van Den Bossche, P.; Omar, N.; Van Mierlo, J. Impact of the temperature in the evaluation of battery performances during long-term cycling—Characterisation and modelling. *Appl. Sci.* **2018**, *8*, 1364. [[CrossRef](#)]
16. Liu, C.; Liu, L. Optimal design of Li-ion batteries through multi-physics modeling and multi-objective optimization. *J. Electrochem. Soc.* **2017**, *164*, 3254–3264. [[CrossRef](#)]
17. Mei, W.; Chen, H.; Sun, J.; Wang, Q. The effect of electrode design parameters on battery performance and optimization of electrode thickness based on the electrochemical–thermal coupling model. *Sustain. Energy Fuels* **2019**, *3*, 148–165. [[CrossRef](#)]
18. Vega-Garita, V.; Ramirez-Elizondo, L.; Bauer, P. Physical integration of a photovoltaic-battery system: A thermal analysis. *Appl. Energy* **2017**, *208*, 446–455. [[CrossRef](#)]
19. Keyser, M.; Pesaran, A.; Li, Q.; Santhanagopalan, S.; Smith, K.; Wood, E.; Ahmed, S.; Bloom, I.; Dufek, E.; Shirk, M.; et al. Enabling fast charging—Battery thermal considerations. *J. Power Sources* **2017**, *367*, 228–236. [[CrossRef](#)]
20. Rahn, C.D.; Wang, C.Y. *Battery Systems Engineering*; John Wiley & Sons Ltd.: Chichester, UK, 2013.
21. Bohn, P.; Liebig, G.; Komsytska, L.; Wittstock, G. Temperature propagation in prismatic lithium-ion-cells after short term thermal stress. *J. Power Sources* **2016**, *313*, 30–36. [[CrossRef](#)]
22. Becker, J.; Nemeth, T.; Wegmann, R.; Sauer, D. Dimensioning and optimization of hybrid Li-ion battery systems for EVs. *World Electr. Veh. J.* **2018**, *9*, 19. [[CrossRef](#)]
23. Liu, H.; Wei, Z.; He, W.; Zhao, J. Thermal issues about Li-ion batteries and recent progress in battery thermal management systems: A review. *Energy Convers. Manag.* **2017**, *150*, 304–330. [[CrossRef](#)]
24. Schweiger, H.G.; Obeidi, O.; Komesker, O.; Raschke, A.; Schiemann, M.; Zehner, C.; Gehnen, M.; Keller, M.; Birke, P. Comparison of several methods for determining the internal resistance of lithium ion cells. *Sensors* **2010**, *10*, 5604–5625. [[CrossRef](#)] [[PubMed](#)]
25. Park, M.; Zhang, X.; Chung, M.; Less, G.B.; Sastry, A.M. A review of conduction phenomena in Li-ion batteries. *J. Power Sources* **2010**, *195*, 7904–7929. [[CrossRef](#)]

26. Viswanathan, V.V.; Choi, D.; Wang, D.; Xu, W.; Towne, S.; Williford, R.E.; Zhang, J.G.; Liu, J.; Yang, Z. Effect of entropy change of lithium intercalation in cathodes and anodes on Li-ion battery thermal management. *J. Power Sources* **2010**, *195*, 3720–3729. [[CrossRef](#)]
27. Thomas, K.E.; Newman, J. Heats of mixing and of entropy in porous insertion electrodes. *J. Power Sources* **2003**, *119*, 844–849. [[CrossRef](#)]
28. Bernardi, D.; Newman, J.; Pawlikowski, E. A general energy balance for battery systems. *J. Electrochem. Soc.* **1985**, *132*. [[CrossRef](#)]
29. Loges, A.; Herberger, S.; Seegert, P.; Wetzel, T. A study on specific heat capacities of Li-ion cell components and their influence on thermal management. *J. Power Sources* **2016**, *336*, 341–350. [[CrossRef](#)]
30. Maleki, H.; Al Hallaj, S.A.H.; Selman, R.; Dinwiddie, R.B.; Wang, H. Thermal properties of lithium-ion battery and components. *J. Electrochem. Soc.* **1999**, *146*, 947. [[CrossRef](#)]
31. Maleki, H.; Wang, H.; Porter, W.; Hallmark, J. Li-Ion polymer cells thermal property changes as a function of cycle-life. *J. Power Sources* **2014**, *263*, 223–230. [[CrossRef](#)]
32. Werner, D.; Loges, A.; Becker, D.J.; Wetzel, T. Thermal conductivity of Li-ion batteries and their electrode configurations—A novel combination of modelling and experimental approach. *J. Power Sources* **2017**, *364*, 72–83. [[CrossRef](#)]
33. Koo, B.; Goli, P.; Sumant, A.V.; Dos Santos Claro, P.C.; Rajh, T.; Johnson, C.S.; Balandin, A.A.; Shevchenko, E.V. Toward lithium ion batteries with enhanced thermal conductivity. *ACS Nano* **2014**, *8*, 7202–7207. [[CrossRef](#)] [[PubMed](#)]
34. Reimers, J.N. Accurate and efficient treatment of foil currents in a spiral wound Li-ion cell. *J. Electrochem. Soc.* **2013**, *161*, 118–127. [[CrossRef](#)]
35. Erhard, S.V.; Osswald, P.J.; Keil, P.; Höffer, E.; Haug, M.; Noel, A.; Wilhelm, J.; Rieger, B.; Schmidt, K.; Kosch, S.; et al. Simulation and measurement of the current density distribution in lithium-ion batteries by a multi-tab cell approach. *J. Electrochem. Soc.* **2017**, *164*, 6324–6333. [[CrossRef](#)]
36. Yi, J.; Kim, U.S.; Shin, C.B.; Han, T.; Park, S. Three-dimensional thermal modeling of a lithium-ion battery considering the combined effects of the electrical and thermal contact resistances between current collecting tab and lead wire. *J. Electrochem. Soc.* **2013**, *160*, 437–443. [[CrossRef](#)]
37. Hales, A.; Diaz, L.B.; Marzook, M.W.; Zhao, Y.; Patel, Y.; Offer, G. The cell cooling coefficient: A standard to define heat rejection from lithium-ion batteries. *J. Electrochem. Soc.* **2019**, *166*, 2383–2395. [[CrossRef](#)]
38. Yu, K.; Yang, X.; Cheng, Y.; Li, C. Thermal analysis and two-directional air flow thermal management for lithium-ion battery pack. *J. Power Sources* **2014**, *270*, 193–200. [[CrossRef](#)]
39. Park, H. A design of air flow configuration for cooling lithium ion battery in hybrid electric vehicles. *J. Power Sources* **2013**, *239*, 30–36. [[CrossRef](#)]
40. Wang, T.; Tseng, K.J.; Zhao, J. Development of efficient air-cooling strategies for lithium-ion battery module based on empirical heat source model. *Appl. Therm. Eng.* **2015**, *90*, 521–529. [[CrossRef](#)]
41. Sun, H.; Dixon, R. Development of a liquid cooled battery module. *J. Electrochem. Soc.* **2016**, *163*, 313–321. [[CrossRef](#)]
42. Zhao, C.; Cao, W.; Dong, T.; Jiang, F. Thermal behavior study of discharging/charging cylindrical lithium-ion battery module cooled by channelled liquid flow. *Int. J. Heat Mass Transf.* **2018**, *120*, 751–762. [[CrossRef](#)]
43. Tran, T.-H.; Harmand, S.; Desmet, B.; Filangi, S. Experimental investigation on the feasibility of heat pipe cooling for HEV/EV lithium-ion battery. *Appl. Therm. Eng.* **2014**, *63*, 551–558. [[CrossRef](#)]
44. Khateeb, S.A.; Amiruddin, S.; Farid, M.; Selman, J.R.; Al-Hallaj, S. Thermal management of Li-ion battery with phase change material for electric scooters: Experimental validation. *J. Power Sources* **2005**, *142*, 345–353. [[CrossRef](#)]
45. Somasundaram, K.; Birgersson, E.; Mujumdar, A.S. Thermal-electrochemical model for passive thermal management of a spiral-wound lithium-ion battery. *J. Power Sources* **2012**, *203*, 84–96. [[CrossRef](#)]
46. Zhao, L.; Wang, J.; Li, Y.; Liu, Q.; Li, W. Experimental investigation of a lithium battery cooling system. *Sustainability* **2019**, *11*, 5020. [[CrossRef](#)]
47. Liebig, G.; Gupta, G.; Kirstein, U.; Schuldt, F.; Agert, C. Parameterization and validation of an electrochemical thermal model of a lithium-ion battery. *Batteries* **2019**, *5*, 62. [[CrossRef](#)]
48. Ecker, M.; Tran, T.K.D.; Dechent, P.; Kabitz, S.; Warnecke, A.; Sauer, D.U. Parameterization of a physico-chemical model of a lithium-ion battery: I. Determination of parameters. *J. Electrochem. Soc.* **2015**, *162*, A1836–A1848. [[CrossRef](#)]

49. Schmalstieg, J.; Rahe, C.; Ecker, M.; Sauer, D.U. Full cell parameterization of a high-power lithium-ion battery for a physico-chemical model: Part I. Physical and electrochemical parameters. *J. Electrochem. Soc.* **2018**, *165*, 3799–3810. [[CrossRef](#)]
50. Dai, H.; Jiang, B.; Wei, X. Impedance characterization and modeling of lithium-ion batteries considering the internal temperature gradient. *Energies* **2018**, *11*, 220. [[CrossRef](#)]
51. Schmalstieg, J.; Sauer, D.U. Full cell parameterization of a high-power lithium-ion battery for a physico-chemical model: Part II. Thermal parameters and validation. *J. Electrochem. Soc.* **2018**, *165*, 3811–3819. [[CrossRef](#)]
52. Ecker, M.; Kabitz, S.; Laresgoiti, I.; Sauer, D.U. Parameterization of a Physico-chemical model of a lithium-ion battery: II. Model validation. *J. Electrochem. Soc.* **2015**, *162*, 1849–1857. [[CrossRef](#)]
53. Erhard, S. Mehrdimensionale Elektrochemisch-Thermische Modellierung Von Lithium-Ionen-Batterien. Ph.D. Thesis, Technische Universität München, Munich, Germany, 2017.
54. Christen, R.; Rizzo, G.; Gadola, A.; Stöck, M. Test method for thermal characterization of Li-ion cells and verification of cooling concepts. *Batteries* **2017**, *3*, 3. [[CrossRef](#)]
55. Wu, B.; Li, Z.; Zhang, J. Thermal design for the pouch-type large-format lithium-ion batteries: I. Thermo-electrical modeling and origins of temperature non-uniformity. *J. Electrochem. Soc.* **2014**, *162*, 181–191. [[CrossRef](#)]
56. Schmalstieg, J. Physikalisch-Elektrochemische Simulation Von Lithium-Ionen-Batterien: Implementierung, Parametrierung und Anwendung. Ph.D. Thesis, RWTH Aachen University, Aachener Beiträge des ISEA, Aachen, Germany, 2017.
57. Ecker, M. Lithium Plating in Lithium-Ion Batteries: An Experimental and Simulation Approach. Ph.D. Thesis, RWTH Aachen University, Aachener Beiträge des ISEA, Aachen, Germany, 2016.
58. Höhne, G.W.H.; Hemminger, W.F.; Flammersheim, H.J. Theoretical fundamentals of differential scanning calorimeters. In *Differential Scanning Calorimetry*; Springer: Berlin, Heidelberg, 2003; pp. 31–63.
59. Parker, W.J.; Jenkins, R.J.; Butler, C.P.; Abbott, G.L. Flash method of determining thermal diffusivity, heat capacity, and thermal conductivity. *J. Appl. Phys.* **1961**, *32*, 1679–1684. [[CrossRef](#)]
60. Kim, S.U.; Albertus, P.; Cook, D.; Monroe, C.W.; Christensen, J. Thermoelectrochemical simulations of performance and abuse in 50-Ah automotive cells. *J. Power Sources* **2014**, *268*, 625–633. [[CrossRef](#)]
61. Pals, C.R.; Newman, J. Thermal modeling of the lithium/polymer battery, I. Discharge behavior of a single cell. *J. Electrochem. Soc.* **1995**, *10*, 3274–3281. [[CrossRef](#)]
62. Zhang, G.; Cao, L.; Ge, S.; Wang, C.Y.; Shaffer, C.E.; Rahn, C.D. In situ measurement of radial temperature distributions in cylindrical Li-ion cells. *J. Electrochem. Soc.* **2014**, *161*, 1499–1507. [[CrossRef](#)]
63. Pop, I.; Ingham, D.B. Chapter 2—Mixed convection boundary-layer flow along a vertical flat plate. In *Convective Heat Transfer*; Pop, I., Ingham, D.B., Eds.; Pergamon: Oxford, UK, 2001; pp. 45–85.
64. Kim, G.H.; Smith, K.; Lee, K.J.; Santhanagopalan, S.; Pesaran, A. Multi-domain modeling of lithium-ion batteries encompassing multi-physics in varied length scales. *J. Electrochem. Soc.* **2011**, *158*, 955. [[CrossRef](#)]
65. Lundgren, H.; Svens, P.; Ekström, H.; Tengstedt, C.; Lindström, J.; Behm, M.; Lindbergh, G. Thermal management of large-format prismatic lithium-ion battery in PHEV application. *J. Electrochem. Soc.* **2015**, *163*, 309–317. [[CrossRef](#)]
66. Optris GmbH. Basic Principles of Non-Contact Temperature Measurement. Available online: https://www.optris.de/lexikon?file=tl_files/pdf/Downloads/Zubehoer/IR-Grundlagen.pdf (accessed on 3 July 2019).
67. Zhang, J.; Wu, B.; Li, Z.; Huang, J. Simultaneous estimation of thermal parameters for large-format laminated lithium-ion batteries. *J. Power Sources* **2014**, *259*, 106–116. [[CrossRef](#)]
68. Touloukian, Y.S.; Liley, P.E.; Saxena, S.C. Thermophysical Properties of Matter—The TPRC Data Series. Volume 3. Thermal Conductivity—Nonmetallic Liquids and Gases. Available online: <https://apps.dtic.mil/dtic/tr/fulltext/u2/a951937.pdf> (accessed on 30 December 2019).
69. Brainard, A.J.; Keenan, J.H.; Chao, J.; Kaye, J. Gas tables: International version second edition (SI units). *AIChE J.* **1984**, *30*, 172. [[CrossRef](#)]
70. Klein, S.A.; Alvarado, F.L. Table Properties of Air at 1 Atm Pressure. Available online: https://www.me.psu.edu/cimbala/me433/Links/Table_A_9_CC_Properties_of_Air.pdf (accessed on 16 October 2019).
71. Lee, K.J.; Smith, K.; Pesaran, A.; Kim, G.H. Three dimensional thermal-, electrical-, and electrochemical-coupled model for cylindrical wound large format lithium-ion batteries. *J. Power Sources* **2013**, *241*, 20–32. [[CrossRef](#)]

72. Bazinski, S.J.; Wang, X. Experimental study on the influence of temperature and state-of-charge on the thermophysical properties of an LFP pouch cell. *J. Power Sources* **2015**, *293*, 283–291. [[CrossRef](#)]
73. Sarge, S.M.; Poeßnecker, W. The influence of heat resistances and heat transfers on the uncertainty of heat-capacity measurements by means of differential scanning calorimetry (DSC). *Thermochim. Acta* **1999**, *329*, 17–21. [[CrossRef](#)]
74. Vertiz, G.; Oyarbide, M.; Macicior, H.; Miguel, O.; Cantero, I.; Fernandez De Arroiate, P.; Ulacia, I. Thermal characterization of large size lithium-ion pouch cell based on 1d electro-thermal model. *J. Power Sources* **2014**, *272*, 476–484. [[CrossRef](#)]
75. Loges, A.; Herberger, S.; Werner, D.; Wetzel, T. Thermal characterization of Li-ion cell electrodes by photothermal deflection spectroscopy. *J. Power Sources* **2016**, *325*, 104–115. [[CrossRef](#)]
76. Jarrett, A.; Kim, I.Y. Influence of operating conditions on the optimum design of electric vehicle battery cooling plates. *J. Power Sources* **2014**, *245*, 644–655. [[CrossRef](#)]
77. Uddin, K.; Perera, S.; Widanage, W.; Somerville, L.; Marco, J. Characterising lithium-ion battery degradation through the identification and tracking of electrochemical battery model parameters. *Batteries* **2016**, *2*, 13. [[CrossRef](#)]
78. Dao, T.S.; Vyasarayani, C.P.; McPhee, J. Simplification and order reduction of lithium-ion battery model based on porous-electrode theory. *J. Power Sources* **2012**, *198*, 329–337. [[CrossRef](#)]
79. Hadigol, M.; Maute, K.; Doostan, A. On uncertainty quantification of lithium-ion batteries: Application to an LiC₆/LiCoO₂ cell. *J. Power Sources* **2015**, *300*, 507–524. [[CrossRef](#)]
80. Liu, G.; Ouyang, M.; Lu, L.; Li, J.; Han, X. Analysis of the heat generation of lithium-ion battery during charging and discharging considering different influencing factors. *J. Therm. Anal. Calorim.* **2014**, *116*, 1001–1010. [[CrossRef](#)]
81. Nyman, A.; Behm, M.; Lindbergh, G. Electrochemical characterisation and modelling of the mass transport phenomena in LiPF₆–EC–EMC electrolyte. *Electrochim. Acta* **2008**, *53*, 6356–6365. [[CrossRef](#)]
82. Zavalis, T.G.; Behm, M.; Lindbergh, G. Investigation of short-circuit scenarios in a lithium-ion battery cell. *J. Electrochem. Soc.* **2012**, *159*, 848–859. [[CrossRef](#)]
83. Pierson, H.O. *Handbook of Carbon, Graphite, Diamonds and Fullerenes—Processing, Properties and Applications*; Noyes Publications: Park Ridge, NJ, USA, 1993.
84. Villars, P.; Cenzual, K. Li[Ni_{1/3}Co_{1/3}Mn_{1/3}]O₂ Crystal Structure: Datasheet from “PAULING FILE Multinaries Edition—2012”. Available online: https://materials.springer.com/isp/crystallographic/docs/sd_1125611 (accessed on 5 September 2019).
85. Von Srbik, M.T.; Marinescu, M.; Martinez-Botas, R.F.; Offer, G.J. A physically meaningful equivalent circuit network model of a lithium-ion battery accounting for local electrochemical and thermal behaviour, variable double layer capacitance and degradation. *J. Power Sources* **2016**, *325*, 171–184. [[CrossRef](#)]



© 2020 by the authors. Licensee MDPI, Basel, Switzerland. This article is an open access article distributed under the terms and conditions of the Creative Commons Attribution (CC BY) license (<http://creativecommons.org/licenses/by/4.0/>).